Chapter 11
Lattice Boltzmann Simulations of Wetting and Drop Dynamics

Halim Kusumaatmaja and Julia M. Yeomans

11.1 Introduction

Recently there has been a huge effort in the scientific community to miniaturise fluidic operations to micron and nanoscales [1]. This has changed the way scientists think about fluids, and it potentially has far-reaching technological implications, analogous to the miniaturization of electronics. The goal is to engineer "lab on a chip" devices, where numerous biological and chemical experiments can be performed rapidly, and in parallel, while consuming little reagent.

An important aspect of the physics of fluids at micron and nanoscales is the increasing relevance of surface effects. Surface slip will dominate flow in nanochannels, and the movement of small drops across a substrate will be strongly affected by the interactions between the fluid and the surface. This has been exploited in the functional adaptation of many biological systems, for example lotus leaves [2], desert beetles [3] and butterfly wings [4]. Moreover, the wetting and spreading of fluids over surfaces is key to numerous technological processes, for example in oil recovery, painting, and inkjet printing.

Small liquid drops are spherical when they are in air, to minimise the surface energy. When placed on a solid the degree to which a drop spreads depends on the balance of interfacial energies between the solid, liquid, and gas phases. In equilibrium the liquid–gas interface maintains a spherical cap profile, and the liquid drop joins the solid at a contact angle θ_e, where

$$\cos\theta_{\mathrm{e}} = \frac{\sigma_{\mathrm{GS}} - \sigma_{\mathrm{LS}}}{\sigma_{\mathrm{LG}}} \tag{11.1}$$

and σ_{GS}, σ_{LS}, and σ_{LG} are the gas–solid, liquid–solid and liquid–gas surface tensions. Equation (11.1) is Young's equation and the equilibrium contact angle is

H. Kusumaatmaja (✉)
Max Planck Institute of Colloids and Interfaces, Science Park Golm, 14424 Potsdam, Germany
e-mail: kusumaatmaja@gmail.com

A.G. Hoekstra et al. (eds.), *Simulating Complex Systems by Cellular Automata*,
Understanding Complex Systems, DOI 10.1007/978-3-642-12203-3_11,
© Springer-Verlag Berlin Heidelberg 2010

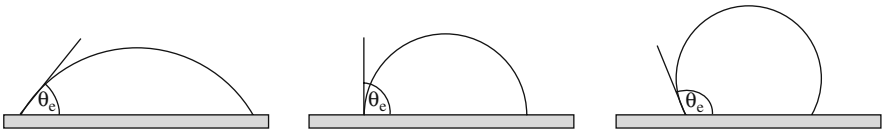

(a) hydrophilic: $\theta_e < 90°$ (b) neutral wetting: $\theta_e = 90°$ (c) hydrophobic: $\theta_e > 90°$

Fig. 11.1 Profile of a liquid drop on (**a**) a hydrophilic, (**b**) a neutrally wetting and (**c**) a hydrophobic surface

often called the Young angle. A solid surface is termed hydrophilic[1] when $\theta_e < 90°$, neutrally wetting when $\theta_e = 90°$ and hydrophobic when $\theta_e > 90°$. This is illustrated in Fig. 11.1. For reviews of wetting and spreading see [5–8].

Wetting phenomena are often further complicated by the fact that the solid surfaces are never perfectly homogeneous. For micron and nanometer drops, the typical length scale of surface heterogeneities can be comparable to the size of the drop itself. Random disorder on a surface is notoriously difficult to describe theoretically or numerically. However, as a result of recent and rapid developments in microfabrication techniques, it is now possible to manufacture surfaces with well controlled patterning on micron, and even nanometer, length scales. The patterning can be either chemical, with the contact angle varying from place to place, or topographical, where the relief of the surface changes. Patterning surfaces leads to a rich range of drop thermodynamics and hydrodynamics which, because the surfaces are well characterised, can now be investigated experimentally.

Analytical solutions describing the behaviour of drops on surfaces are possible in some special cases, but in general they are not tractable when the surface heterogeneities are taken into account. Therefore there is a need for powerful numerical techniques that are able to both solve the hydrodynamic equations of motion of the fluids, and to take into account the effect of surface patterning, with relative ease. To this end, in this chapter, we introduce a mesoscale numerical algorithm, the lattice Boltzmann method, and show how it may be used to investigate the physics of wetting and spreading.

Writing down an algorithm which solves the Navier-Stokes equations is rather easy. This is because these equations are based on local conservation of mass and momentum and, as long as the conservation laws are represented correctly, (and space is discretised in a sufficiently symmetric way) the hydrodynamic equations will be recovered in the continuum limit. This was pointed out by Frisch et al. [9] who wrote down the first mesoscale algorithm for the Navier-Stokes equation. This was a lattice-gas cellular automaton: particles move on a lattice and collide at the nodes according to rules which impose mass and momentum conservation. As long as the lattice has sufficient symmetry it is possible to choose collision rules that reproduce the Navier-Stokes equation in the continuum limit.

[1] Strictly, the terms hydrophilic and hydrophobic are appropriate only when the liquid is water. Nonetheless, they are often used more generally.

Cellular automata models of hydrodynamics have proved important in many contexts but can be difficult to use because of large fluctuations in macroscopic quantities such as the density and the velocity. The need to average over the fluctuations can cancel out the advantage of an algorithm which is easy to parallelise. However many other mesoscale methods have evolved from the ideas of cellular automata, and one of these is the lattice Boltzmann approach [10–13]. The discrete variables used in cellular automata are replaced by a set of distribution functions that represent the average population of fluid particles. This removes the difficulty of fluctuations: lattice Boltzmann can be viewed as a mean-field version of the cellular automata models.

Lattice Boltzmann algorithms can be extended to multiphase and complex fluids [14–16]. The algorithm solves the Navier-Stokes equations and, as we shall describe below, the thermodynamic properties of a given fluid and its interactions with a surface can be modelled rather easily by introducing a free energy functional that is minimised in equilibrium. Moreover, lattice Boltzmann algorithms are well able to handle flow in complex geometries and hence represent an efficient numerical way of treating surfaces with topographic patterning.

The chapter comprises two parts. First, in Sects. 11.2, 11.3, and 11.4 we explain the physical model and the lattice Boltzmann algorithm used to solve it. We introduce a free energy functional for a binary fluid [17, 18] and explain how it handles the essential ingredients needed to describe wetting phenomena; phase separation, surface tension and contact angles. The generalisation of the Navier-Stokes equations appropriate for the two-phase system are summarised. We then describe lattice Boltzmann algorithms that will solve the hydrodynamic equations, commenting particularly on the thermodynamic and hydrodynamic boundary conditions needed to model wetting. Next, in Sects. 11.5, 11.6, and 11.7, we illustrate the efficacy of the algorithm by describing several applications to the physics of drops on smooth and patterned surfaces. These include capillary filling, viscous fingering, controlling drop motion using chemical patterning, slip in patterned microchannels and superhydrophobic surfaces.

11.2 The Binary Model

11.2.1 Thermodynamics of the Fluid

To model drops of fluid on a surface we need first to describe their equilibrium properties, such as binary fluid coexistence, surface tension and contact angle. As we are working on micron-length scales we can use a continuum, Landau free energy [17], which is minimised in equilibrium,

$$\Psi = \int_V \left(\psi_b + \frac{\kappa}{2} (\partial_\alpha \phi)^2 \right) dV + \int_S \psi_s \, dS, \tag{11.2}$$

where the bulk free energy density ψ_b is taken to have the form

$$\psi_b = \frac{c^2}{3} n \ln n + A\left(-\tfrac{1}{2}\phi^2 + \tfrac{1}{4}\phi^4\right). \tag{11.3}$$

n is the fluid density which is chosen to be 1 everywhere, ϕ is the order parameter and $c = \Delta x/\Delta t$, where Δx and Δt represent the discretisation in space and time respectively. This choice of ψ_b gives binary phase separation into two phases with $\phi_\alpha = 1$ and $\phi_\beta = -1$, where α and β label the two coexisting bulk phases.

The second and third terms in Eq. (11.2) are needed to account for the fluid–fluid and fluid–solid surface tensions. Let us first consider the fluid–fluid surface tension and for simplicity, restrict ourselves to one dimension. Minimising the volume terms in the free energy functional with respect to ϕ leads to the condition for equilibrium

$$\mu \equiv -A\phi + A\phi^3 - \kappa \frac{d^2}{dx^2}\phi = 0 \tag{11.4}$$

where μ is the chemical potential. Equation (11.4) allows an interface solution of the form

$$\phi = \tanh\left(\frac{x}{\sqrt{2}\xi}\right) \tag{11.5}$$

where $\xi = \sqrt{\kappa/A}$ is defined as the interface width. Since this must typically be chosen of order a few lattice spacings in a simulation, models of this type are often called diffuse interface models [19, 20].

Using Noether's theorem, we find that

$$\psi_b - \frac{\kappa}{2}\left(\frac{d\phi}{dx}\right)^2 = \text{constant} = \psi_b|_{\phi=\pm 1}\,. \tag{11.6}$$

We can therefore define the excess bulk free energy density as

$$W = \psi_b - \psi_b|_{\phi=\pm 1} = \tfrac{A}{2}\left(\phi^2 - 1\right)^2 = \frac{\kappa}{2}\left(\frac{d\phi}{dx}\right)^2. \tag{11.7}$$

The surface tension, γ, of the liquid–liquid interface can be calculated by integrating the sum of the excess bulk free energy density and the second (κ) term in Eq. (11.2)

$$\gamma = \int_{\phi_\beta}^{\phi_\alpha} \left(W + \frac{\kappa}{2}\left(\frac{d\phi}{dx}\right)^2\right) dx = \int_{\phi_\beta}^{\phi_\alpha} \kappa \left(\frac{d\phi}{dx}\right)^2 dx = \sqrt{8\kappa A/9}. \tag{11.8}$$

The second integral in Eq. (11.2) is over the system's solid surface and is used to describe the interactions between the fluid and the surface. Following Cahn [21], the surface energy density is taken to be $\psi_s = -h\phi_s$, where ϕ_s is the value of the order

parameter at the surface. Minimisation of the free energy shows that the gradient in ϕ at the solid boundary is

$$\kappa \frac{d\phi}{dx} = -\frac{d\psi_s}{d\phi_s} = -h\,. \tag{11.9}$$

Equation (11.9) can be used together with Eq. (11.7) to determine ϕ_s.

The fluid–solid surface tensions can be calculated in a similar way to the fluid–fluid surface tension, except that now we also have to take into account the contributions from the surface energy term.

$$\gamma_{s\alpha} = -h\phi_{s\alpha} + \int_{\phi_{s\alpha}}^{\phi_\alpha} \kappa \left(\frac{d\phi}{dx}\right)^2 dx = \frac{\gamma}{2} - \frac{\gamma}{2}(1+\Omega)^{3/2}\,, \tag{11.10}$$

$$\gamma_{s\beta} = -h\phi_{s\beta} + \int_{\phi_{s\beta}}^{\phi_\beta} \kappa \left(\frac{d\phi}{dx}\right)^2 dx = \frac{\gamma}{2} - \frac{\gamma}{2}(1-\Omega)^{3/2}\,, \tag{11.11}$$

where $\Omega = \sqrt{\frac{2}{\kappa A}}h$. The notations $\phi_{s\alpha}$ and $\phi_{s\beta}$ stand for the values of the order parameter at the surface for phases α and β respectively.

The contact angle follows from substituting the values of the surface tensions into Young's law, Eq. (11.1), to give (with θ_e defined as the contact angle of the α-phase)

$$\cos\theta_e = \frac{\gamma_{s\beta} - \gamma_{s\alpha}}{\gamma} = \frac{(1+\Omega)^{3/2} - (1-\Omega)^{3/2}}{2}\,. \tag{11.12}$$

Equation (11.12) can be inverted to give a relation between the phenomenological parameter h and the equilibrium contact angle θ_e [17]

$$h = \sqrt{2\kappa A}\ \mathrm{sign}\left(\frac{\pi}{2} - \theta_e\right)\sqrt{\cos\left(\frac{\alpha}{3}\right)\left\{1 - \cos\left(\frac{\alpha}{3}\right)\right\}}\,, \tag{11.13}$$

where $\alpha = \cos^{-1}\left(\sin^2\theta_e\right)$ and the function sign returns the sign of its argument.

Lattice Boltzmann simulation results for the equilibrium contact angle of a liquid drop on a smooth solid surface are shown in Fig. 11.2. The exact result, given by Eq. (11.13), is also shown for comparison. Deviation is only noticeable at small contact angles. This discrepancy is mainly because the finite width of the interface, which is neglected when assuming that the drop is a spherical cap, becomes comparable to the height of the drop.

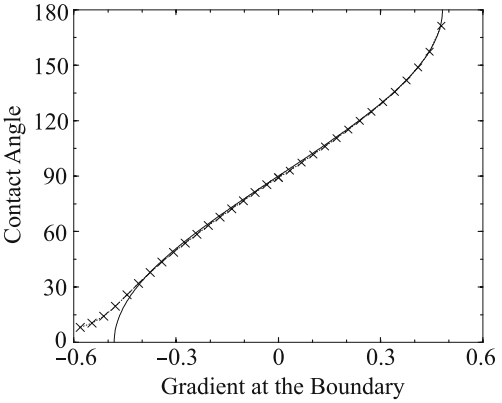

Fig. 11.2 The equilibrium contact angle as a function of the gradient in ϕ at the boundary. Crosses are lattice Boltzmann simulation results, while the *solid curve* is the theoretical expression, Eq. (11.13). We have used A = 0.04 and κ = 0.04 Reprinted figure with permission from Pooley et al. [18]. Copyright (2008) by the American Physical Society

11.3 Hydrodynamics of the Fluid

The hydrodynamic equations of motion for the binary fluid are the continuity equation (11.14), the Navier-Stokes equation (11.15) and the convection-diffusion equation (11.16)

$$\partial_t n + \partial_\alpha (n v_\alpha) = 0\,, \tag{11.14}$$

$$\begin{aligned}\partial_t (n v_\alpha) + \partial_\beta (n v_\alpha v_\beta) = &-\partial_\beta P_{\alpha\beta} + \partial_\beta [n\nu(\partial_\beta v_\alpha + \partial_\alpha v_\beta) \\ &+ \left(n\lambda \delta_{\alpha\beta} \partial_\gamma v_\gamma\right)] + n a_\alpha\,,\end{aligned} \tag{11.15}$$

$$\partial_t \phi + \partial_\alpha (\phi v_\alpha) = M \nabla^2 \mu \tag{11.16}$$

where $\mathbf{v}$, $\mathbf{P}$, ν, $\mathbf{a}$ and M are the local velocity, pressure tensor, shear kinematic viscosity, acceleration provided by the body force and mobility respectively. The bulk kinematic viscosity is $\lambda + \frac{d}{2}\nu$, where d is the dimension of the system.

The equilibrium properties of the fluid appear in the equations of motion through the chemical potential defined in Eq. (11.4) while the pressure can be derived from the free energy

$$\partial_\beta P_{\alpha\beta} = n \partial_\alpha \left(\tfrac{\delta \psi_b}{\delta n}\right) + \phi \partial_\alpha \left(\tfrac{\delta \psi_b}{\delta \phi}\right). \tag{11.17}$$

Using the definition of ψ_b in Eq. (11.3), it follows that [17]

$$P_{\alpha\beta} = \left(p_b - \frac{\kappa}{2}(\partial_\gamma \phi)^2 - \kappa \phi \partial_{\gamma\gamma} \phi\right) \delta_{\alpha\beta} + \kappa (\partial_\alpha \phi)(\partial_\beta \phi)\,, \tag{11.18}$$

$$p_b = \tfrac{c^2}{3} n + A \left(-\tfrac{1}{2}\phi^2 + \tfrac{3}{4}\phi^4\right). \tag{11.19}$$

p_b is the bulk pressure term which is related to the speed of sound in the model via $c_s^2 = \frac{dp_b}{dn} = \frac{c^2}{3}$. Equilibrium corresponds to $\partial_\beta P_{\alpha\beta} = 0$.

It is also important to note that the finite interface width allows slip to be generated close to the contact line by diffusive transport across the interface [17–20]. Slip is needed to remove the stress singularity at the moving contact line (see e.g. [22–24]). In this model it is controlled by the mobility parameter M.

11.4 The Lattice Boltzmann Algorithm

We now define a lattice Boltmann algorithm which solves Eqs. (11.14), (11.15), and (11.16). The basic idea behind lattice Boltzmann algorithms is to associate distribution functions, discrete in time and space, to a set of velocity directions $\mathbf{e}_i$. For example, for a three-dimensional, 19-velocity model, the lattice velocities are chosen to be

$$\begin{pmatrix} e_{x0\text{-}6} \\ e_{y0\text{-}6} \\ e_{z0\text{-}6} \end{pmatrix} = \begin{bmatrix} 0 & c & -c & 0 & 0 & 0 & 0 \\ 0 & 0 & 0 & c & -c & 0 & 0 \\ 0 & 0 & 0 & 0 & 0 & c & -c \end{bmatrix}, \tag{11.20}$$

$$\begin{pmatrix} e_{x7\text{-}18} \\ e_{y7\text{-}18} \\ e_{z7\text{-}18} \end{pmatrix} = \begin{bmatrix} c & -c & c & -c & 0 & 0 & 0 & 0 & c & -c & c & -c \\ c & c & -c & -c & c & -c & c & -c & 0 & 0 & 0 & 0 \\ 0 & 0 & 0 & 0 & c & c & -c & -c & c & c & -c & -c \end{bmatrix}.$$

c, the lattice velocity, is defined by $c = \Delta x/\Delta t$. The directions of the velocity vectors are shown in Fig. 11.3.

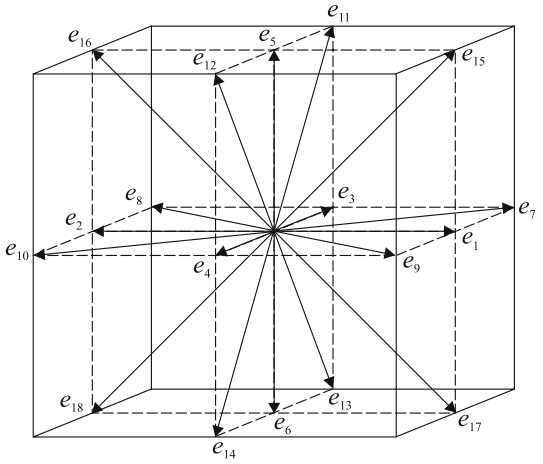

Fig. 11.3 The directions of the lattice velocity vectors in the 19-velocity lattice Boltzmann model

We need to define two distribution functions, $f_i(\mathbf{r}, t)$ and $g_i(\mathbf{r}, t)$, to describe a binary fluid. The physical variables are related to the distribution functions by

$$n = \sum_i f_i, \quad nu_\alpha = \sum_i f_i e_{i\alpha}, \quad \phi = \sum_i g_i, \tag{11.21}$$

where $\mathbf{u}$ is defined as $\mathbf{u} = \mathbf{v} - \mathbf{a}\Delta t/2$, and $\mathbf{a}$ is the acceleration associated with any applied body force. (This distinction between $\mathbf{u}$ and $\mathbf{v}$ is required so that the lattice Boltzmann equation recovers the continuity (11.14) and Navier-Stokes (11.15) equations in the continuum limit in a system with an applied force. In practice, the value of $\mathbf{v}$ is typically two to three order of magnitudes larger than $\mathbf{a}\Delta t$ in most simulations. Hence the distinction between $\mathbf{u}$ and $\mathbf{v}$ can usually be neglected.)

The time evolution equations for the particle distribution functions, using the standard BGK approximation [25], can be broken down into two steps

$$\begin{aligned}
\text{Collision step}: \quad & f_i'(\mathbf{r}, t) = f_i(\mathbf{r}, t) - \tfrac{1}{\tau}\left[f_i(\mathbf{r}, t) - f_i^{\mathrm{eq}}(\mathbf{r}, t)\right] + F_i(\mathbf{r}, t)\,, \\
& g_i'(\mathbf{r}, t) = g_i(\mathbf{r}, t) - \tfrac{1}{\tau_\phi}\left[g_i(\mathbf{r}, t) - g_i^{\mathrm{eq}}(\mathbf{r}, t)\right], \\
\text{Propagation step}: \quad & f_i(\mathbf{r} + \mathbf{e}_i\Delta t, t + \Delta t) = f_i'(\mathbf{r}, t)\,, \\
& g_i(\mathbf{r} + \mathbf{e}_i\Delta t, t + \Delta t) = g_i'(\mathbf{r}, t)
\end{aligned} \tag{11.22}$$

where f_i^{eq} and g_i^{eq} are local equilibrium distribution functions, defined as a power series in the velocity, τ and τ_ϕ are the relaxation times and F_i is a term that corresponds to an external body force. It can be shown, using a Taylor expansion, that Eqs. (11.22) reproduce Eqs. (11.14), (11.15) and (11.16) in the continuum limit if the correct thermodynamic and hydrodynamic information is input to the simulation by a suitable choice of local equilibrium functions and forcing terms. Details of the derivation can be found in e.g. [10–14]. The constraints that need to be satisfied are

$$\sum_i f_i^{\mathrm{eq}} = n\,, \quad \sum_i f_i^{\mathrm{eq}} e_{i\alpha} = n v_\alpha\,, \tag{11.23}$$

$$\sum_i f_i^{\mathrm{eq}} e_{i\alpha} e_{i\beta} = P_{\alpha\beta} + n v_\alpha v_\beta\,, \tag{11.24}$$

$$\sum_i f_i^{\mathrm{eq}} e_{i\alpha} e_{i\beta} e_{i\gamma} = \frac{nc^2}{3}[v_\alpha\delta_{\beta\gamma} + v_\beta\delta_{\gamma\alpha} + v_\gamma\delta_{\alpha\beta}]\,, \tag{11.25}$$

$$\sum_i g_i^{\mathrm{eq}} = \phi\,, \quad \sum_i g_i^{\mathrm{eq}} e_{i\alpha} = \phi v_\alpha\,, \tag{11.26}$$

$$\sum_i g_i^{\mathrm{eq}} e_{i\alpha} e_{i\beta} = \Gamma\mu\delta_{\alpha\beta} + \phi v_\alpha v_\beta\,. \tag{11.27}$$

$$\sum_i F_i = 0\,, \quad \sum_i F_i e_{i\alpha} = \Delta t\left(1 - \frac{1}{2\tau}\right) n a_\alpha\,, \tag{11.28}$$

$$\sum_i F_i e_{i\alpha} e_{i\beta} = \Delta t \left(1 - \frac{1}{2\tau}\right)(n v_\alpha a_\beta + n v_\beta a_\alpha). \tag{11.29}$$

Note that Eqs. (11.23) and the first equation in (11.26) correspond to conservation of mass, momentum and concentration.

A possible choice for f_i^{eq}, g_i^{eq} and F_i that satisfies the constraints (11.23), (11.24), (11.25), (11.26), (11.27), (11.28) and (11.29) is a power series expansion in the velocity [26, 27]

$$\begin{aligned}
f_i^{\mathrm{eq}} &= \frac{w_i}{c^2}\Big(p_b - \kappa\phi\nabla^2\phi + e_{i\alpha} n v_\alpha + \tfrac{3}{2c^2}\left[e_{i\alpha}e_{i\beta} - \tfrac{c^2}{3}\delta_{\alpha\beta}\right] \\
&\quad \times\Big(n v_\alpha v_\beta + \lambda\left[v_\alpha \partial_\beta n + v_\beta \partial_\alpha n + \delta_{\alpha\beta} v_\gamma \partial_\gamma n\right]\Big)\Big) \\
&\quad + \frac{\kappa}{c^2}\Big(w_i^{xx}\partial_x\phi\partial_x\phi + w_i^{yy}\partial_y\phi\partial_y\phi + w_i^{zz}\partial_z\phi\partial_z\phi) \\
&\quad + \frac{\kappa}{c^2}\Big(w_i^{xy}\partial_x\phi\partial_y\phi + w_i^{yz}\partial_y\phi\partial_z\phi + w_i^{zx}\partial_z\phi\partial_x\phi\Big), \qquad (11.30) \\
g_i^{\mathrm{eq}} &= \frac{w_i}{c^2}\Big(\Gamma\mu + e_{i\alpha}\phi v_\alpha + \tfrac{3}{2c^2}\left[e_{i\alpha}e_{i\beta} - \tfrac{c^2}{3}\delta_{\alpha\beta}\right]\phi v_\alpha v_\beta\Big), \\
F_i &= \Delta t \frac{w_i}{c^2}\left(1 - \frac{1}{2\tau}\right)\left[e_{i\alpha} n a_\alpha + \frac{3}{2c^2}\left(e_{i\alpha}e_{i\beta} - \frac{c^2}{3}\delta_{\alpha\beta}\right)(n v_\alpha a_\beta + n v_\beta a_\alpha)\right].
\end{aligned}$$

where a choice for the w_i aimed at minimising spurious velocities[2] is [26]

$$\begin{aligned}
w_{1\text{-}6} &= \tfrac{1}{6}, \quad w_{7\text{-}18} = \tfrac{1}{12}, \\
w_{1,2}^{xx} &= w_{3,4}^{yy} = w_{5,6}^{zz} = \tfrac{5}{12}, \\
w_{3\text{-}6}^{xx} &= w_{1,2,5,6}^{yy} = w_{1\text{-}4}^{zz} = -\tfrac{1}{3}, \\
w_{7\text{-}10}^{xx} &= w_{15\text{-}18}^{xx} = w_{7\text{-}14}^{yy} = w_{11\text{-}18}^{zz} = -\tfrac{1}{24}, \\
w_{11\text{-}14}^{xx} &= w_{15\text{-}18}^{yy} = w_{7\text{-}10}^{zz} = \tfrac{1}{12}, \\
w_{1\text{-}6}^{xy} &= w_{1\text{-}6}^{yz} = w_{1\text{-}6}^{zx} = 0, \\
w_{7,10}^{xy} &= w_{11,14}^{yz} = w_{15,18}^{zx} = \tfrac{1}{4}, \\
w_{8,9}^{xy} &= w_{12,13}^{yz} = w_{16,17}^{zx} = -\tfrac{1}{4}, \\
w_{11\text{-}18}^{xy} &= w_{7\text{-}10}^{yz} = w_{15\text{-}18}^{yz} = w_{7\text{-}14}^{zx} = 0
\end{aligned}$$

[2] These are small velocities which remain in equilibrium. They are a consequence of discretisation errors, see Sect. 4.1.

The relaxation parameters τ and τ_ϕ in the lattice Boltzmann algorithm are related to the parameters in the hydrodynamic equations ν, λ and M through

$$\nu = (c^2 \Delta t(\tau - 1/2))/3\,, \tag{11.31}$$

$$\lambda = \nu(1 - 3c_s^2/c^2)\,, \tag{11.32}$$

$$M = \Delta t \Gamma \left(\tau_\phi - \tfrac{1}{2}\right), \tag{11.33}$$

where Γ is a tunable parameter that appears in the equilibrium distribution. Since ν, λ and M are positive quantities, the values of the relaxation times τ and τ_ϕ have to be larger than $1/2$.

In a typical binary lattice Boltzmann simulation, there are four important parameters controlling the physics: the length scale of the system L, the viscosity η, the surface tension γ, and the body force $n\mathbf{a}$. To match these to physical values we can choose only three quantities; a length scale L_o, a time scale T_o, and a mass scale M_o which are further constrained by the stability of the simulations. Therefore the simulation parameters cannot be arbitrarily matched to an experiment. In practice, a useful approach can be to determine L_o, T_o, and M_o by matching L, η and γ between simulations and experiments, and then to use these scales to determine the appropriate value of $n\mathbf{a}$. (A simulation parameter with dimensions $[L]^{n1}[T]^{n2}[M]^{n3}$ is multiplied by $L_o^{n1}\, T_o^{n2}\, M_o^{n3}$ to give the physical value.)

11.4.1 The Multiple Relaxation Time Algorithm

Figure 11.2 shows that there is excellent agreement between the theoretical value of the contact angle for a given surface field and that calculated numerically. However, these results were obtained using a relaxation time $\tau = 1$. For values of τ significantly different to unity the agreement is less good [18]. This discrepancy is caused by strong spurious velocities near the contact point which continuously push the system out of equilibrium and result in the deformation of the interface. The spurious velocities, which are a result of discretisation errors, are common to all lattice-based solutions of the Navier-Stokes equations, but are particularly pronounced near interfaces and surfaces. Taking $\tau = 1$ damps out many of the spurious contributions [18].

Since, in wetting problems, the two fluids generally have different viscosities (for example, the viscosities of water and air differ by a factor of 1000), restriction to $\tau = 1$ imposes a serious limitation. However the problem can be remedied by using a multiple relaxation time lattice Boltzmann algorithm [18].

The idea behind the multiple relaxation time lattice Boltzmann method [28–30] is that different relaxation parameters are used for different linear combinations of the distribution functions. The relaxation term $\frac{1}{\tau}\left[f_i - f_i^{\mathrm{eq}}\right]$ on the right hand side of the lattice Boltzmann equation for f_i (11.22) is replaced by

$$\mathbf{M}^{-1}\mathbf{S}\mathbf{M}\left[\mathbf{f}-\mathbf{f}^{\mathrm{eq}}\right], \tag{11.34}$$

where the particle distributions f_i and f_i^{eq} are written as column vectors and $\mathbf{M}$ is the matrix [28]

$$\mathbf{M}=\begin{pmatrix}
1 & 1 & 1 & 1 & 1 & 1 & 1 & 1 & 1 & 1 & 1 & 1 & 1 & 1 & 1 & 1 & 1 & 1 & 1\\
-30 & -11 & -11 & -11 & -11 & -11 & -11 & 8 & 8 & 8 & 8 & 8 & 8 & 8 & 8 & 8 & 8 & 8 & 8\\
12 & -4 & -4 & -4 & -4 & -4 & -4 & 1 & 1 & 1 & 1 & 1 & 1 & 1 & 1 & 1 & 1 & 1 & 1\\
0 & 1 & -1 & 0 & 0 & 0 & 0 & 1 & -1 & 1 & -1 & 0 & 0 & 0 & 0 & 1 & -1 & 1 & -1\\
0 & -4 & 4 & 0 & 0 & 0 & 0 & 1 & -1 & 1 & -1 & 0 & 0 & 0 & 0 & 1 & -1 & 1 & -1\\
0 & 0 & 0 & 1 & -1 & 0 & 0 & 1 & 1 & -1 & -1 & 1 & -1 & 1 & -1 & 0 & 0 & 0 & 0\\
0 & 0 & 0 & -4 & 4 & 0 & 0 & 1 & 1 & -1 & -1 & 1 & -1 & 1 & -1 & 0 & 0 & 0 & 0\\
0 & 0 & 0 & 0 & 0 & 1 & -1 & 0 & 0 & 0 & 0 & 1 & 1 & -1 & -1 & 1 & 1 & -1 & -1\\
0 & 0 & 0 & 0 & 0 & -4 & 4 & 0 & 0 & 0 & 0 & 1 & 1 & -1 & -1 & 1 & 1 & -1 & -1\\
0 & 2 & 2 & -1 & -1 & -1 & -1 & 1 & 1 & 1 & 1 & -2 & -2 & -2 & -2 & 1 & 1 & 1 & 1\\
0 & -4 & -4 & 2 & 2 & 2 & 2 & 1 & 1 & 1 & 1 & -2 & -2 & -2 & -2 & 1 & 1 & 1 & 1\\
0 & 0 & 0 & 1 & 1 & -1 & -1 & 1 & 1 & 1 & 1 & 0 & 0 & 0 & 0 & -1 & -1 & -1 & -1\\
0 & 0 & 0 & -2 & -2 & 2 & 2 & 1 & 1 & 1 & 1 & 0 & 0 & 0 & 0 & -1 & -1 & -1 & -1\\
0 & 0 & 0 & 0 & 0 & 0 & 0 & 1 & -1 & -1 & 1 & 0 & 0 & 0 & 0 & 0 & 0 & 0 & 0\\
0 & 0 & 0 & 0 & 0 & 0 & 0 & 0 & 0 & 0 & 0 & 1 & -1 & -1 & 1 & 0 & 0 & 0 & 0\\
0 & 0 & 0 & 0 & 0 & 0 & 0 & 0 & 0 & 0 & 0 & 0 & 0 & 0 & 0 & 1 & -1 & -1 & 1\\
0 & 0 & 0 & 0 & 0 & 0 & 0 & 1 & -1 & 1 & -1 & 0 & 0 & 0 & 0 & -1 & 1 & -1 & 1\\
0 & 0 & 0 & 0 & 0 & 0 & 0 & -1 & -1 & 1 & 1 & 1 & -1 & 1 & -1 & 0 & 0 & 0 & 0\\
0 & 0 & 0 & 0 & 0 & 0 & 0 & 0 & 0 & 0 & 0 & -1 & -1 & 1 & 1 & 1 & 1 & -1 & -1
\end{pmatrix}. \tag{11.35}$$

Each of the rows in $\mathbf{M}$ is mutually orthogonal so the inverse follows easily as

$$\mathbf{M}^{-1}_{ij}=\frac{1}{\sum_k \mathbf{M}^2_{jk}}\mathbf{M}_{ji}\,. \tag{11.36}$$

The matrix $\mathbf{M}$ performs a change of basis. The new basis is designed to contain more physically relevant variables. For example the first row corresponds to the density n. Similarly, the fourth, sixth and eighth lines calculate the momentum densities nu_x, nu_y and nu_z respectively. These are the conserved moments. The 10th, 12th, 14th, 15th, 16th lines correspond to the components of the symmetric, traceless, viscous stress tensor $3\sigma_{xx}$, $\sigma_{yy}-\sigma_{zz}$, σ_{xy}, σ_{yz} and σ_{xz}. The other terms do not contain any real physical meaning and they are often called the ghost modes.

The matrix $\mathbf{S}$ in Eq. (11.34) is diagonal and contains the information about how fast each variable relaxes at each time step. A useful choice is [28]

$$\mathbf{S}=\mathrm{diag}\,(0,1,1,0,1,0,1,0,1,\omega,1,\omega,1,\omega,\omega,\omega,1,1,1)\,, \tag{11.37}$$

where $\omega = 1/\tau$ now determines the fluid viscosities ν and λ. Note that some of the elements of $\mathbf{S}$ are zero. This choice is arbitrary as these modes correspond to the conserved moments, for which $M_{ji}\left[f_i - f_i^{\mathrm{eq}}\right] = 0\,(j = 0, 3, 5, 7)$. Using unity for the remaining, ghost, modes minimises the spurious velocities. This is an acceptable choice because these modes do not correspond to physical variables.

For a system with variable viscosity it would seem necessary to recalculate the collision matrix $\mathbf{C} = \mathbf{M}^{-1}\mathbf{S}\mathbf{M}$ at each lattice node and at each time-step. This is very demanding computationally. One practical approach to overcome this difficulty is to create a lookup table for various values of the viscosity.

11.4.2 Boundary Conditions

In a typical lattice Boltzmann simulation of a wetting problem there are two important boundary conditions: the wetting boundary condition, given by Eq. (11.9), and the no-slip boundary condition on the fluid velocity. While these boundary conditions are simple conceptually, their implementation can be tricky for complex geometries.

One way to implement the no-slip condition is a linear interpolation bounce back rule proposed by Bouzidi et al. [31]. A schematic diagram illustrating this approach, for the one dimensional case and the $f_i(\mathbf{r}, t)$ distribution function, is shown in Fig. 11.4a. In one dimension, there are two distribution functions, $f_1[\mathrm{k}]$ and $f_2[\mathrm{k}]$, for a given lattice node k. When the node k is located to the right of a wall, as shown in Fig. 11.4a, the function $f_1^*[\mathrm{k}]$ is undetermined after the propagation step. (To clarify notation we use * to denotes distribution functions after propagation.) To determine $f_1^*[\mathrm{k}]$, Bouzidi et al. consider two cases. If the distance of the wall from the fluid node, d_{wall}, is less than half of a lattice spacing, $f_1^*[\mathrm{k}]$ is chosen to be a weighted average of $f_2[\mathrm{k}]$ and $f_2[\mathrm{k+1}]$. If, however, d_{wall} is more than half of a lattice spacing $f_1^*[\mathrm{k}]$ is interpolated from $f_2[\mathrm{k}]$ and $f_1[\mathrm{k}]$:

$$\begin{aligned} d_{\mathrm{wall}} < 0.5 &: f_1^*[\mathrm{k}] = f_2[\mathrm{k}] \times 2d_{\mathrm{wall}} + f_2[\mathrm{k}+1] \times (1 - 2d_{\mathrm{wall}})\,, \\ d_{\mathrm{wall}} > 0.5 &: f_1^*[\mathrm{k}] = f_2[\mathrm{k}]/(2d_{\mathrm{wall}}) + f_1[\mathrm{k}] \times (1 - 1/(2d_{\mathrm{wall}}))\,. \end{aligned} \tag{11.37}$$

The bounce back rules for the other lattice directions in higher dimensions, and for the $g_i(\mathbf{r}, t)$ distribution function, are applied in exactly the same way (with d_{wall} normalised to the lattice spacing in the relevant direction). This ensures that there is no momentum flux parallel to the wall and that the no-slip boundary condition is satisfied at the position of the wall. It was shown by Ginzburg and d'Humières [32] that this no-slip boundary is accurate to the second order.

When the velocity of the wall is non-zero, for example when one wants to investigate a shear flow, the bounce back rule should be modified by adding the following terms [31]:

$$\begin{aligned} d_{\mathrm{wall}} < 0.5 &: \Delta f = -2\,n\,w_i\,(\mathbf{e}_i \cdot \mathbf{v}_{\mathrm{wall}}) \\ &\quad\; \Delta g = -2\,\phi\,w_i\,(\mathbf{e}_i \cdot \mathbf{v}_{\mathrm{wall}}) \end{aligned}$$

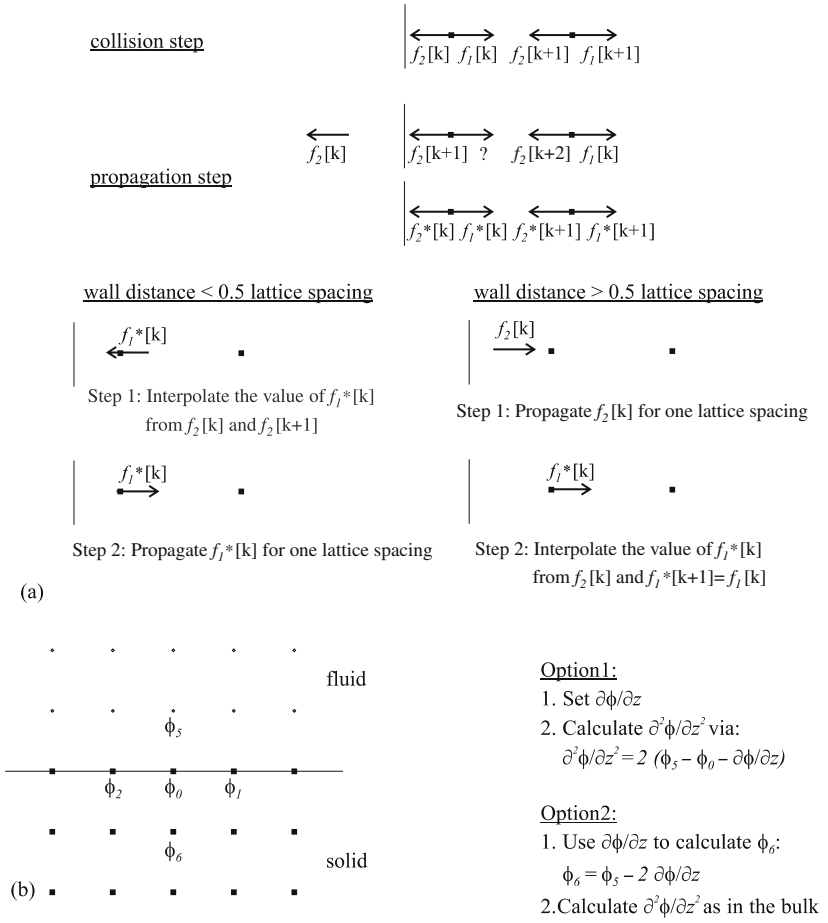

Fig. 11.4 Schematic diagram of the no-slip and wetting boundary conditions. (**a**) Link bounce back rule. (**b**) Implementations of the wetting boundary condition

$$d_{\text{wall}} > 0.5 : \Delta f = -n\, w_i / d_{\text{wall}}\, (\mathbf{e}_i \cdot \mathbf{v}_{\text{wall}})$$
$$\Delta g = -\phi\, w_i / d_{\text{wall}}\, (\mathbf{e}_i \cdot \mathbf{v}_{\text{wall}})$$

where w_i and $\mathbf{e}_i$ are the weight coefficient and the lattice velocity direction of the distribution functions before being bounced off the wall (e.g. in Eq. (11.37), this would correspond to w_2 and $\mathbf{e}_2$).

We next describe two ways to implement the wetting boundary condition. Equation (11.9) sets the value of the first derivative $\partial\phi/\partial z|_0$ at the surface, but an estimate of the second derivative is also required to calculate the equilibrium distribution function (11.30). Our explanations refer to the labelling of lattice nodes in Fig. 11.4b, for an interface perpendicular to the z-axis.

In a first method, $\partial\phi/\partial z$ is set to take the value given by Eq. (11.9) at the ϕ_0 lattice node and $\partial^2\phi/\partial z^2$ is calculated by Taylor expanding ϕ_5 with respect to ϕ_0 and neglecting third and higher derivatives in ϕ,

$$\partial^2\phi/\partial z^2|_0 = 2 \times (\phi_5 - \phi_0 - \partial\phi/\partial z|_0)\,. \tag{11.38}$$

The main advantage of this implementation is it is not necessary to simulate any solid nodes.

An alternative implentation of the wetting boundary condition is to assign appropriate density values to the solid nodes neighbouring the boundary, so that Eq. (11.9) is satisfied. In the schematic diagram shown in Fig. 11.4c, this corresponds to assigning[3]

$$\phi_6 = \phi_5 - 2\,\partial\phi/\partial z|_0\ . \tag{11.39}$$

The main advantage of this approach is that $\nabla^2\phi$ can be calculated in exactly the same way at the surface as in the bulk. Furthermore, since all the nearest and next nearest neighbour nodes of any surface site have appropriate density values, better accuracy can be achieved by choosing the best stencil to calculate derivatives [26].

For more complex geometries, for example surfaces which do not follow a lattice axis or corners, the wetting boundary conditions can be implemented in a similar way. This typically gives a set of linear equations that must be solved simultaneously.

Finally we summarise an algorithm that we have found to work well for simulating the dynamics of the contact line in fluids where the two components have different viscosities [18]:

Step 1: Calculate the density, concentration and velocity using the moments described in Eqs. (11.21).
Step 2: Set the velocity of the boundary nodes to zero, or more generally to the velocity of the wall. This reduces spurious velocities introduced by the bounce-back boundary conditions.
Step 3: Implement the wetting boundary condition by setting the first and second derivatives of the order parameter.
Step 4: Calculate the equilibrium distribution function and use the multiple relaxation time lattice Boltzmann method to perform the collision step.
Step 5: Perform the streaming step with the bounce back rule at the boundaries (Eq. (11.37)).

[3] If the wall is located at the mid-link between ϕ_5 and ϕ_0, appropriate wetting boundary conditions can be implemented by setting $\phi_0 = \phi_5 - \partial\phi/\partial z|_0$.

11.4.3 Other Lattice Boltzmann Algorithms

The lattice Boltzmann implementations we have described in this section are not unique, and many authors have proposed alternative approaches to solve the equations of motion of multiphase fluids. For example:

1. Phase ordering can be imposed by using an effective interaction, rather than a free energy [15, 33].
2. The thermodynamics leading to phase ordering can be included in the lattice Boltzmann scheme as a forcing term, rather than as a correction to the pressure in the second moment of the equilibrium distribution function [33, 34].
3. Different sets of velocity vectors can be defined [35, 36].
4. The forms of f^{eq}, g^{eq}, and F that satisfy the hydrodynamic equations of motion in the continuum limit are not unique [27, 35, 36]. It is useful to exploit this to minimise spurious currents [26].
5. There are many ways of implementing the hydrodynamic boundary conditions [32, 37–39].

11.5 Smooth Walls

In the next three sections, we shall describe a number of examples where lattice Boltzmann simulations have proved successful in providing insights to wetting phenomena. We start with two problems where the solid boundaries are assumed to be flat and homogeneous. Firstly, we discuss the capillary penetration of a wetting fluid [40], and secondly, we look at the classical problem of fingering instabilities in narrow channels [41]. These are both relevant in many industrial and biological systems, and they play an increasingly important role in many microfluidic devices. We then explain, in Sects. 11.6 and 11.7 how chemical and topographical heterogeneities on a surface may lead to complex drop morphologies that depend sensitively on the details of the surface patterning, as well as the path by which the system is prepared[4].

11.5.1 Capillary Filling

When a liquid is brought into contact with a small capillary tube, it will penetrate the capillary provided that this lowers its surface energy i.e. when the capillary is hydrophilic with respect to the liquid. The classical analysis of the dynamics of

[4] Some of the results in Sects. 11.5, 11.6, and 11.7 were obtained using a lattice Boltzmann algorithm for a one-component, liquid–gas system rather than a two-component fluid. Details of this algorithm are given in [39, 42]. In the one-component model contact line slip occurs because of evaporation and condensation, which is rapid because of the unphysically wide interface. This can lead to unphysical dynamics [43–45].

capillary filling is due to Lucas [46] and Washburn [47]. Consider a capillary of height h with an infinite reservoir of liquid of dynamic viscosity $\eta = n\nu$ at one end. Assuming that the penetrating liquid adopts a parabolic profile, it will fill the capillary with a mean velocity

$$\bar{v} = -\frac{h^2}{12\eta}\frac{dp}{dx} \tag{11.40}$$

where $\frac{dp}{dx}$ is the pressure gradient that sets up the flow. The driving force for the filling is provided by the decrease in free energy as the fluid wets the walls or, equivalently, by the Laplace pressure across the curved liquid–gas interface. Hence

$$\frac{dp}{dx} = -\frac{\gamma}{Rl} \tag{11.41}$$

where $R = h/2\cos\theta^a$ is the radius of curvature of the interface and l is the length of liquid in the tube. Eliminating $\frac{dp}{dx}$ from Eqs. (11.40) and (11.41) and identifying $\bar{v} = dl/dt$ gives the Lucas-Washburn law

$$l = \left(\sigma_{\mathrm{LG}} h \cos\theta^a/3\eta\right)^{1/2} (t + t_0)^{1/2} \tag{11.42}$$

where t_0 is an integration constant.

In Eq. (11.42) it is appropriate to use, not the static, but the advancing contact angle θ^a, as this controls the curvature of the interface and hence the Laplace pressure. The Lucas-Washburn law assumes that there is no resistance to motion from any fluid already in the capillary. Therefore it applies only if the dynamic viscosity of the invading phase η_A is large compared to that of the displaced fluid η_B. If the dissipation in the displaced fluid is taken into account the modified Lucas-Washburn law becomes

$$\eta_A \frac{l^2}{2} + \eta_B \left(Ll - \frac{l^2}{2}\right) = \frac{\sigma_{\mathrm{LG}} h \cos\theta^a}{6}(t + t_0) \tag{11.43}$$

where L is the total length of the capillary.

Numerical results showing capillary filling of a smooth channel are presented in Fig. 11.5. The plot is for a channel of length $L = 640$, infinite width and height $h = 50$. Reservoirs (480×200) of components A and B are attached at each end of the capillary. The two reservoirs are connected to ensure that they have the same pressure. The parameters of the model are chosen so that $\theta_{\mathrm{e}} = 60°$, $\gamma = 0.0188$, $\eta_{\mathrm{A}} = 0.83$, $\eta_{\mathrm{B}} = 0.03$ and $M = 0.05$. The solid line in Fig. 11.5a is a fit to the Lucas-Washburn law using the measured value of the advancing contact angle and correcting for the small viscosity of the displaced B-component. The fit is excellent, except very close to the beginning of the simulation, where deviations due to inertial effects and a non-Poiseuille flow profile are expected.

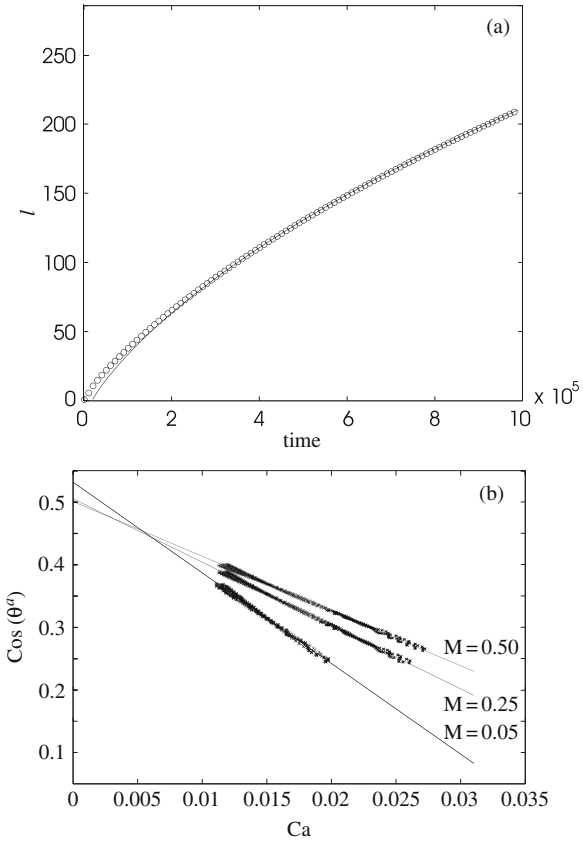

Fig. 11.5 (**a**) Distance a fluid–fluid interface moves along a capillary as a function of time. *Circles* are the lattice Boltzmann simulation results. The *solid line* is a fit to the Lucas-Washburn law using the measured advancing contact angle and correcting for the small viscosity of the displaced component. (**b**) The advancing contact angle of the liquid–liquid interface as a function of the capillary number. The *crosses* are simulation results and the *solid lines* are linear fits of $\cos\theta^a$ to the capillary number [48]. Reprinted figures with permission from Kusumaatmaja, [40] and Pooley, [18]. Copyright (2008) by the American Physical Society

To lowest order in the capillary number, Ca$= v^I \nu/\gamma_{LG}$ where v^I is the interface velocity, the advancing contact angle is related to the equilibrium angle and the capillary number by [48]

$$\cos\theta^a = \cos\theta^{\mathrm{eq}} - \mathrm{Ca}\log(KL/l_{\mathrm{s}}) \tag{11.44}$$

where K is a constant, L is the length scale of the system and l_{s} is the effective slip length at the three phase contact line. Figure 11.5b shows the expected linear dependence, and that the advancing contact angle tends to the correct value as Ca $\to 0$; We obtain $\theta^a|_{Ca\to 0} = 58^\circ$, 60° and 60° for $M = 0.05$, 0.1 and 0.5 respectively.

Note that the slope of the graph, and hence the slip length, depend on the mobility M. This occurs because in diffuse interface models of binary fluids the contact line singularity is relieved by inter-diffusion of the two fluid components [17].

11.5.2 Viscous Fingering

We have just considered the rate at which a viscous fluid displaces a liquid of low viscosity when the driving force is the hydrophilic nature of the channel walls. In such a case, the fluid–fluid interface is stable and has the form of a meniscus. The situation is, however, more complicated when a less viscous fluid is driven to displace a more viscous one, as the interface can now be unstable. If the fluids are moving in the narrow gap between two parallel plates this instability gives rise to the well-known Saffman-Taylor [49] fingers. A typical experiment showing the development of a finger is shown in Fig. 11.6 [50].

Usually the Saffman-Taylor instability is treated as a two dimensional problem, taking an average over the distance between the bounding plates. However the third dimension can affect the way in which the finger forms. Ledesma-Aguilar et al. [41] studied the three dimensional motion, using binary lattice Boltzmann simulations, and found that there are two distinct regimes. If the contact line is able to keep up with the leading interface of the finger (which will happen, at higher Peclet numbers, if the diffusion is sufficiently strong [51]), the fluid-fluid interface retains the form of a meniscus in the direction, z say, between the plates and it is possible to treat

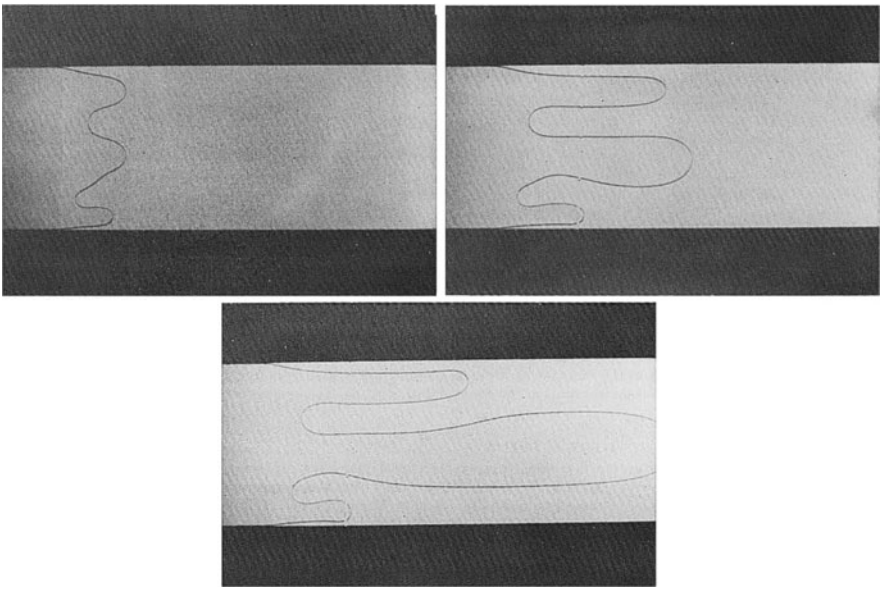

Fig. 11.6 Time evolution of a Saffman-Taylor finger. Reprinted with permission from Tabeling et al. [50, pp. 67–82]. Copyright 1987 Cambridge University Press

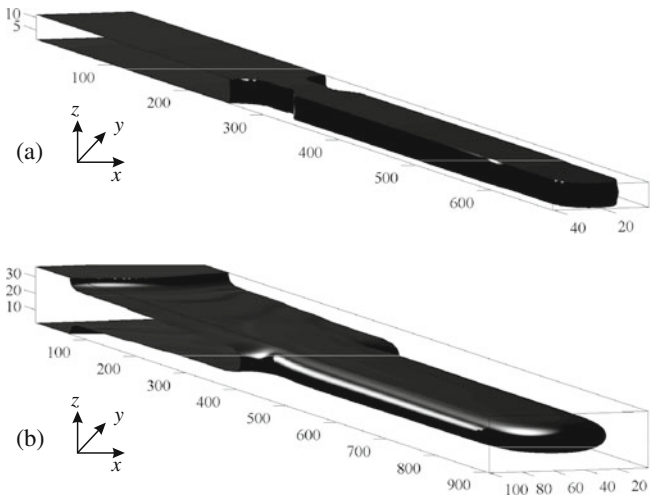

Fig. 11.7 Saffman-Taylor instabilities in the (**a**) meniscus and (**b**) surface film regimes. (**a**) When diffusion is sufficiently strong (high Peclet number), the fluid–fluid interface retains the form of a meniscus in the direction between the plates and the problem is essentially two-dimensional. (b) At low Peclet number, the contact line falls behind and a layer of the displaced phase is formed close to the plates. This means that the advancing fluid forms a finger-like structure in both the x-y and the x-z planes (We thank Ioannis Zacharoudiou for these figures.)

the problem two-dimensionally. At low Peclet numbers the contact line falls behind and a layer of the displaced phase is formed close to the plates. This means that the advancing fluid forms a finger-like structure in both the x-y and the x-z planes. Simulation results showing the shape of the interface in the meniscus and surface film regime are shown in Fig. 11.7.

11.6 Chemical Patterning

We now describe examples where a lattice Boltzmann approach has been used to model drops spreading on chemically patterned surfaces. This is particularly exciting at present because it is becoming increasingly feasible to fabricate surfaces with heterogeneities in a controlled and reproducible manner, allowing surface patterning to be used as a part of a designer toolbox to control the shapes and dynamics of small liquid drops [8, 52, 53]. Variation in the surface wettability can be implemented easily in the lattice Boltzmann simulations by applying different values of the phenomenological parameter h in Eq. (11.13) at different surface lattice sites. However, it is important to note that the typical length scale of the variation in h has to be larger than the interface width of the model.

We first look at a drop spreading on a chemically patterned surface. For a homogeneous surface, the final state is a spherical cap with a contact angle equals to the Young angle. This is not the case for heterogeneous surfaces. Depending on the

initial conditions of the system, the drop can take several metastable states, with shapes that may vary considerably from spherical [8, 52–54].

We then consider two examples where simulations suggest how chemical patterning might be applied to solve industrial problems. In the first [55], we show how a (relatively) hydrophobic grid can be used to alleviate mottle [56] in ink-jet printing. In the second example, we demonstrate that chemical patterning can be used to control drop size and polydispersity [57].

11.6.1 Spreading on a Chemically Striped Surface

Figure 11.8 compares experiments and simulations of drops on a chemically patterned substrate. The surface is lined with relatively hydrophilic and hydrophobic stripes with contact angles 5° and 64° and widths 26 and 47 μm respectively. Figure 11.8a shows the final state of drops jetted onto the surface. The drops' volumes were chosen so that their final diameters were comparable to the stripe width. It is apparent from the figure that the drops can take two final configurations, "diamond"-like and "butterfly"-like.

Figure 11.8b shows simulations of the same system, with parameters chosen so that length scales, surface tension, contact angles, fluid viscosity and liquid density correspond to those of the experiment. Again the diamond and butterfly configurations are observed at long times. The simulations allowed us to follow the dynamics of the liquid drops' motion in detail. In particular, we found that the final drop shape is selected by the initial impact position and velocity. If the drop can touch two neighbouring hydrophilic stripes as it spreads, it will reach the butterfly configuration; if not it will retract back to the diamond pattern, spanning a single stripe.

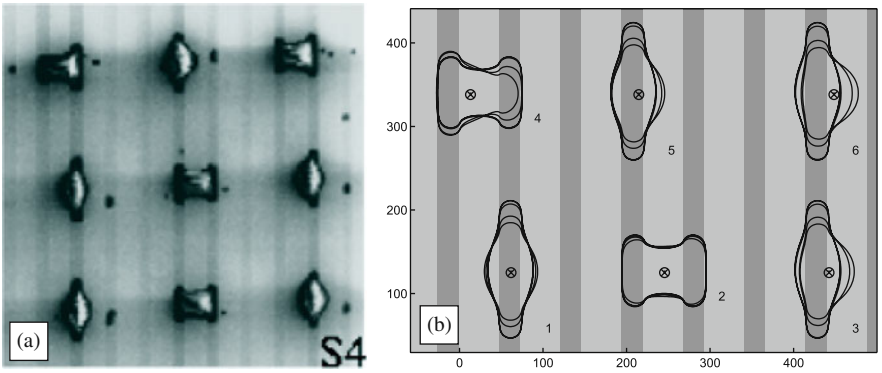

Fig. 11.8 Drops spreading on a chemically striped surface. (**a**) Scanning electron micrographs of ink-jetted drops. (**b**) Numerical simulations of drops hitting the surface at various impact points, indicated by *encircled crosses*. For each drop the faint lines represent the extent of the base of the drop as it evolves and the *bold line* depicts its final shape. Relatively hydrophilic and hydrophobic stripes appear dark and pale, respectively. Reprinted with permission from Léopoldès et al. [54, pp. 9818–9822]. Copyright 2003 American Chemical Society

This can be seen in Fig. 11.8b, where the faint lines show the time evolution of the base of the drop and the solid lines its final shape. Both states are free energy minima but one of the two is a metastable minimum: which one is sensitive to the exact choice of the physical parameters.

11.6.2 Using Chemical Patterning to Control Drop Positioning

An inkjet printed image is produced by jetting an array of micron-scale liquid drops onto a surface. To achieve a solid colour the aim is that the drops, which are jetted at a distance apart comparable to their diameter, should coalesce to form a uniform covering of ink. However, in practice, irregular coalescence due to surface imperfections and randomness in the positions of the jetted drops can dominate. This leads to the formation of large, irregular drops with areas of bare substrate between them as shown in the upper part of Fig. 11.9b. Such configurations lead to poor image quality, called mottle [56].

Figure 11.9a shows that irregular coalescence can be overcome by using a grid of (relatively) hydrophobic chemical stripes. Here the drop has an initial radius of 15 μm and the substrate has contact angle 5°. The hydrophobic grid has stripes of width 6 μm, separated by 66 μm, and contact angle 65°. The simulation shows that the drop is confined even when its initial point of impact is close to the corner of a square.

Results from an experiment demonstrating a similar effect are shown in Fig. 11.9b. The ink drops have a radius $R = 30\,\mu$m and they are jetted in a 50 μm $\times$ 50 μm array. In the upper part of the figure there is no hydrophobic grid and a mottled final configuration is observed. The lower part of Fig. 11.9b carries hydrophobic stripes of 5 μm width forming squares of side 40 μm. The drops now form a more regular pattern determined by the grid.

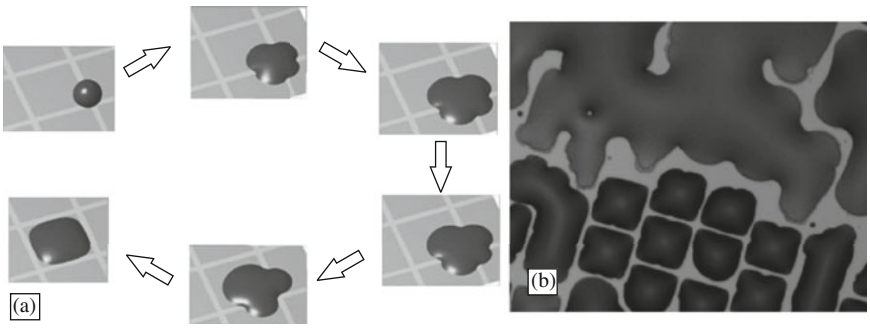

Fig. 11.9 Control of drop position using chemical patterning. (**a**) Time evolution of a drop jetted onto a substrate patterned by a grid. Relatively hydrophobic and hydrophilic areas are *light grey* stripes (65°) and *dark grey* areas (5°) respectively. (**b**) Inkjet drops jetted onto a substrate and cured: (*top*) homogeneous surface and (*bottom*) surface patterned by a relatively hydrophobic grid. Reprinted with permission from Dupuis et al. [55]. Copyright 2005 American Institute of Physics

11.6.3 Using Chemical Patterning to Sort Drop by Size

It is often desirable in microfluidic devices to be able to manipulate and control the motion of liquid drops (see [1] and the references therein). Here we demonstrate a particular example where chemical patterning may be used to sort drops according to their size. The schematic diagram of the system is shown in Fig. 11.10. The surface is patterned with a rectangular grid of hydrophilic (relative to the background) stripes, and a drop is input to the device at A and subject to a body force at an angle $< 45^\circ$ to the x-axis.

The path taken by the drop through the device depends on the drop contact angles with the substrate and on the strength of the body force. It also, of particular relevance to us here, depends on the width of the stripes relative to the drop radius. Figure 11.11a–c show simulations of the paths of drops of initial radius $R = 25, 26$ and 29 moving through such a device. In cases where the drops are confined in the δ_1 stripe, they will move in the x-direction from A to the cross-junction B, where their paths may diverge. In order for a drop to move in the y-direction, the capillary force in this direction must be large enough to overcome the sum of the capillary force and the excess external body force in the x-direction (recall $a_x > a_y$). This is where the asymmetry of the drop shape comes into play. As the volume of the drop is increased, a larger fraction of it overhangs the stripes and hence a larger fraction will interact with the hydrophilic stripe along the y-direction at the junction. This increases the capillary force along y and means that larger drops (e.g. $R > 26$) will move in the y-direction to point C, whereas smaller drops (e.g. $R = 25$) will continue to move along x. By choosing the stripes along the y direction to be of equal widths, but those along x to increase in width with increasing y, it is possible to move the larger drops further along y. As one can see from Fig. 11.11, the drops

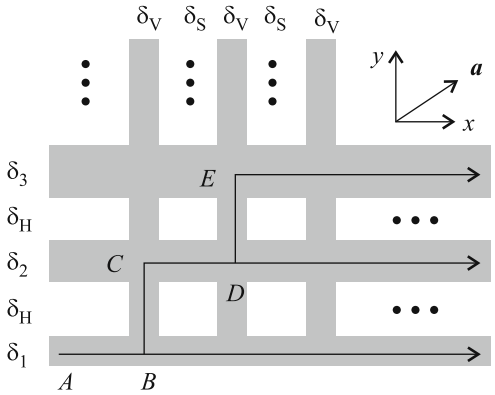

Fig. 11.10 Schematic diagram of a drop sorter. The *grey* stripes on the surface are hydrophilic with respect to the background. δ labels the widths of the stripes and $\boldsymbol{a}$ the imposed acceleration. The *arrows* show possible paths of a drop through the device. Reprinted with permission from Kusumaatmaja and Yeomans [57, pp. 956–959]. Copyright 2007 American Chemical Society

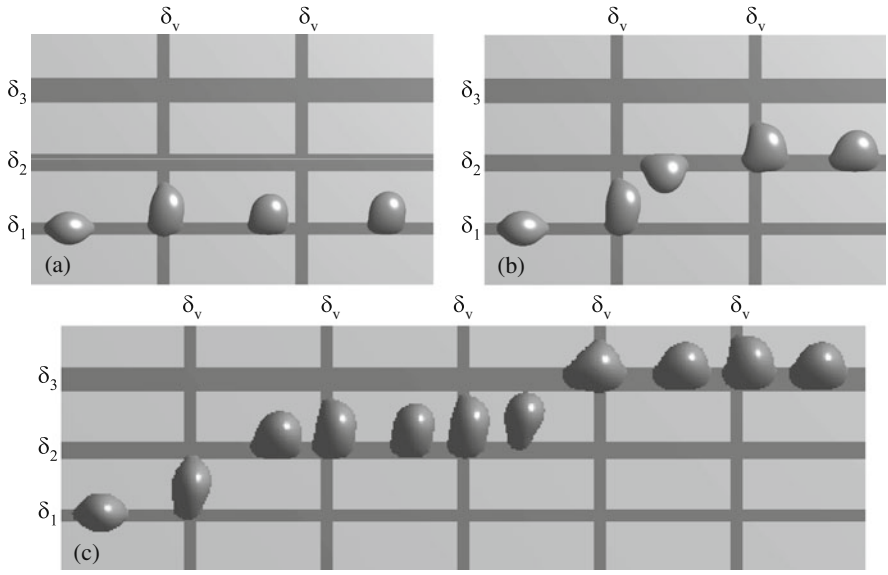

Fig. 11.11 Paths taken by drops of radius (**a**) $R = 25$, (**b**) $R = 26$, and (**c**) $R = 29$ through the drop sorter. $\delta_1 = 20$, $\delta_2 = 30$, $\delta_3 = 40$, and $\delta_V = 20$. Reprinted with permission from Kusumaatmaja and Yeomans [57, pp. 956–959]. Copyright 2007 American Chemical Society

of initial radius $R = 26$ and $R = 29$ are finally confined in the second and third stripe respectively.

These simulations suggest that by increasing the number of stripes and carefully controlling their widths it may be possible to sort polydisperse drops into collections of monodisperse drops. Two other parameters, the wettability contrast and the external body force, could also be adjusted to fine-tune the device.

11.7 Topographical Patterning: Superhydrophobic Surfaces

Superhydrophobic surfaces are a prime example of how heterogeneities can alter the wettability of a surface. On a smooth hydrophobic surface, the highest contact angle that can be achieved is of order 120–130° [6, 58] attainable for, for example, a water drop spreading on fluorinated solids. When the hydrophobic surface is made rough, however, higher contact angles are possible. Several natural materials exhibit this, so-called, superhydrophobicity. Examples include the leaves of the lotus plant [2], butterfly wings [4], water strider legs [59] and duck feathers [60]. Many research groups have now fabricated superhydrophobic surfaces by patterning hydrophobic surfaces with regular posts [58, 61, 62] or with nano-hairs [63]. Indeed superhydrophobicity is a surprisingly robust phenomenon, which requires neither careful patterning nor intrinsic hydrophobicity of the surface material [64, 65].

It is possible to distinguish two ways in which a drop can behave on a superhydrophobic surface. When the drop is suspended on top of the surface roughness, as shown in Fig. 11.12b, the substrate is effectively a composite of liquid–solid and liquid–gas areas. We shall use Φ to denote the area fraction of the liquid–solid contact. If the length scale of the patterning is much smaller than the drop size, the effective liquid–solid surface tension is then $\Phi\,\gamma_{LS} + (1-\Phi)\,\gamma_{LG}$, while the effective gas–solid surface tension is $\Phi\,\gamma_{GS}$. Substituting these into the Young equation (11.1), gives the Cassie-Baxter formula [60]

$$\cos\theta_{\mathrm{CB}} = \Phi\cos\theta_{\mathrm{e}} - (1-\Phi)\,. \tag{11.45}$$

This configuration is called the suspended or Cassie-Baxter state.

If, on the other hand, the liquid drop fills the space between the posts, as shown in Fig. 11.12b, the drop is said to lie in the collapsed or Wenzel state. Both the

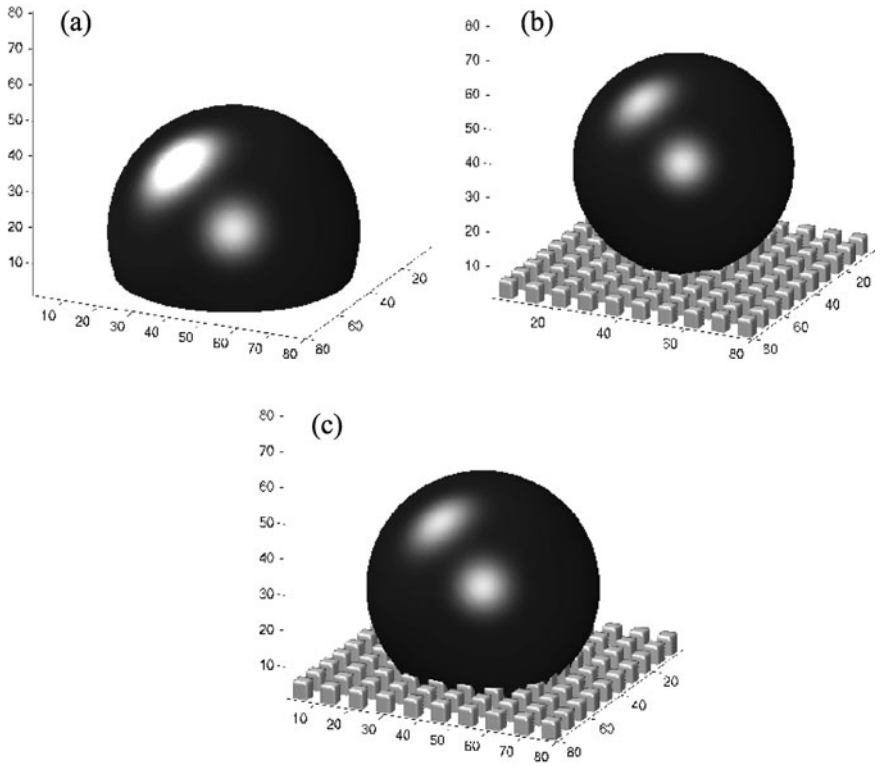

Fig. 11.12 Final states of a spreading drop on (**a**) a hydrophobic surface (**b**) a superhydrophobic surface with the drop suspended (**c**) a superhydrophobic surface with the drop collapsed. Reprinted with permission from Dupuis and Yeomans [39, pp. 2624–2629]. Copyright 2005 American Chemical Society

liquid–solid and gas–solid contact areas are increased by a roughness factor r and the macroscopic contact angle is therefore given by the Wenzel equation [66]

$$\cos\theta_{\mathrm{W}} = r\cos\theta_{\mathrm{e}}\,. \tag{11.46}$$

Figure 11.12 shows simulation results for the final state of a drop of radius $R = 30$ which has spread on a smooth (Fig. 11.12a) and a superhydrophobic surface (Fig. 11.12b and c). A contact angle $\theta_{\mathrm{e}} = 110°$ is set on every surface site. The resultant macroscopic contact angles in the simulations are 110°, 156° and 130° for the flat surface, suspended drop and collapsed drop respectively. The values for the suspended and collapsed drop are compatible with the ones obtained from the Cassie-Baxter and Wenzel formulae, but they are not exactly the same. There are two reasons for this. Firstly, the drop only covers a small number of posts in the simulations. Secondly, the surface inhomogeneities result in the existence of multiple local free energy minima, not just that prescribed by the Cassie-Baxter or Wenzel formulae. This can cause pinning of the contact line and lead to values of contact angles which depend not only on the thermodynamic variables describing the state of the drop, but also on the path by which that state was achieved. This phenomenon, contact angle hysteresis, is well known [5, 67–70], but has suprising consequence for drops on superhydrophobic substrates. We now describe these in more detail.

11.7.1 Contact Line Pinning and Contact Angle Hysteresis

Both chemical and topographical surface patterning may pin the contact line. This can results in variation in the value of the contact angle around a drop. It can also lead to hysteresis, a dependence of the drop shape on its dynamical history. A useful approach to quantify contact angle hysteresis is to slowly increase the volume of a drop until it starts to spread. The contact angle at this moment is termed the advancing angle. Similarly, if the drop volume is slowly reduced, it will start to retreat across the surface at the receding contact angle. The difference between the advancing and receding angles is termed the contact angle hysteresis. However, it should be cautioned that this is not a unique definition; the advancing and receding angles will depend on the direction, relative to the surface patterning, in which they are measured. Moreover the difference in contact angles between the advancing and receding edge of a moving drop will not necessarily be the same as the value measured quasistatically.

This concept of pinning, and of the resulting advancing and receding contact angles, is illustrated in Fig. 11.13 for a drop crossing a ridge. For the contact line to advance, it has to wet the sides of the grooves (Fig. 11.13a) which, according to the Gibb's criterion [71], occurs when the contact angle is locally equal to the Young angle. Therefore the advancing angle (measured with respect to the surface) is $\theta^a = \theta_{\mathrm{e}} + 90°$ for rectangular ridges and, more generally $\theta^a = \theta_{\mathrm{e}} + \alpha$ [70–72] for a surface of maximum inclination α. Similarly, for the contact line to recede,

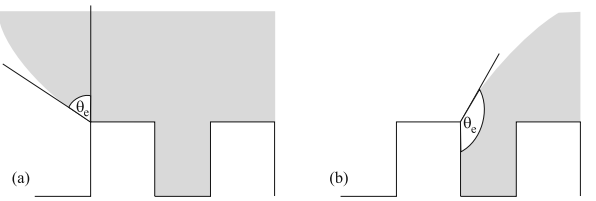

Fig. 11.13 Graphical illustration of the pinning of an (**a**) advancing and (**b**) receding contact line on a surface patterned with *square* ridges

the drop has to dewet the sides of the posts (Fig. 11.13b). This is possible when $\theta^r = \theta_e - 90°$ for rectangular ridges and $\theta^r = \theta_e - \alpha$ [70–72] in general.

Applying these criteria in the context of a two-dimensional drop on a superhydrophobic surface patterned with square posts gives surprising results. For the suspended state $\theta^a = 180°$, the upper limit for the value of the contact angle, and $\theta^r = \theta_e$. For the collapsed drop $\theta^a = 180°$ and $\theta^r = \theta_e - 90°$. In three dimensions we obtain the same qualitative behaviour, though there may be a decrease in the value for the advancing angle and an increase in that for the receding angle because of curvature contributions to the free energy [73].

We now consider Boltzmann simulations [73], showing that they are able to capture contact line pinning and hysteresis. Figure 11.14a and b show the simulation results for a cylindrical (two-dimensional) suspended drop on a superhydrophobic surface comprising regularly spaced posts. In this set of simulations, we used post width = 7, post separation = 13, and an equilibrium contact angle $\theta_e = 120°$. Even after the drop volume was increased quasistatically by a factor ~ 4, and the drop contact angle had reached 162°, no interface depinning transition was observed. After this point, it was no longer possible to continue running the simulations, as the drop filled the simulation box. As the drop volume was slowly decreased, however, the contact line depinned and jumped back across the posts at $\theta^r = 120°$ as predicted analytically.

We now discuss hysteresis for a cylindrical collapsed drop, where the gaps between the posts are filled with liquid. When the drop volume is increased, the drop behaves in the same way as for the suspended state and no contact line motion between posts is observed during the simulation. This is because locally, in the vicinity of the contact line, the drop has no information as to whether it is in the collapsed or suspended state. Typical behavior as the drop volume is decreased is shown in Fig. 11.14c. As for the suspended drop, the contact line is pinned at the outer edge of a post until $\theta = \theta_e$. It then retreats smoothly across the post. However, unlike the suspended case, the contact line is pinned again, at the inner edge of the posts. At this point, the drop is found to recede at 32°, consistent with the expected analytical result $\theta_e - 90° = 30°$.

Even in this simple two-dimensional model, the contact angle hysteresis is much larger for the collapsed state than for the suspended state. This result has an important consequence that, although the static contact angle is increased in both the Wenzel and the Cassie-Baxter states, their dynamical behaviors are very different.

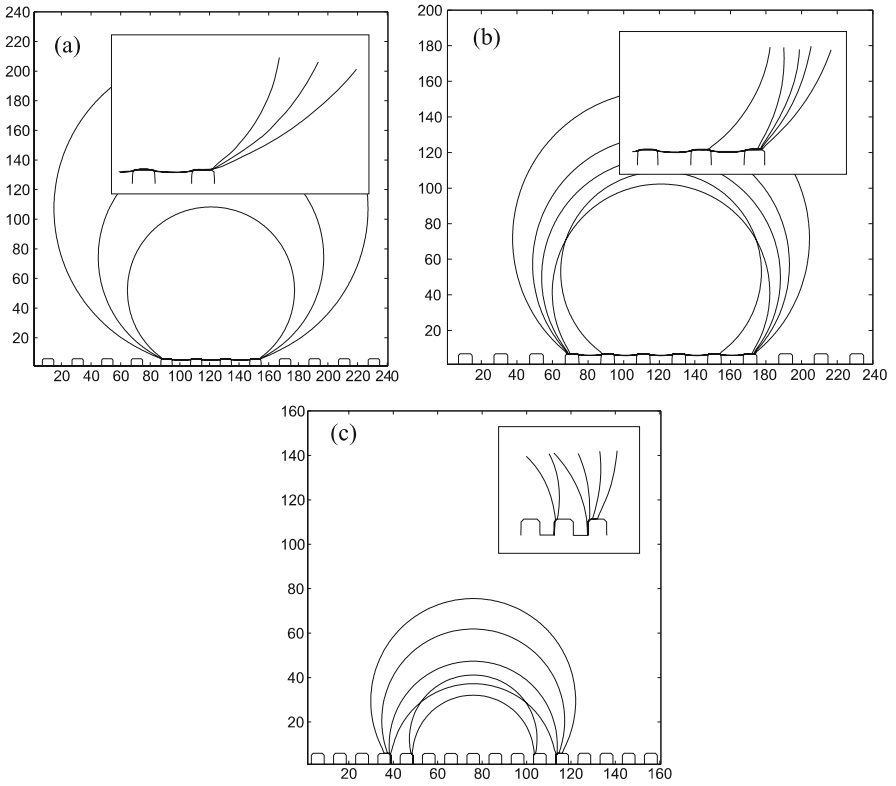

Fig. 11.14 Drop shape as a function of time from lattice Boltzmann simulations of a cylindrical drop (**a**-**b**) suspended and (**c**) collapsed on a topographically patterned surface. (**a**) The advancing contact line remains pinned during the simulation. (**b**) The receding contact line is pinned until $\theta^r \sim 120°$. (**c**) In the collapsed state, the receding contact line is pinned strongly at the inner edge of the posts. The position of the contact lines can be seen more clearly in the *insets*. Reprinted with permission from Kusumaatmaja and Yeomans [73, pp. 6019–6032]. Copyright 2007 American Chemical Society

A liquid drop in the suspended state is very mobile, while that in the collapsed state is very immobile [6, 58].

11.7.2 The Slip Length of Superhydrophobic Surfaces

Another aspect where the dynamics of fluids moving across superhydrophobic surfaces differs between the suspended and the collapsed states is in the value of the slip length. Consider a single phase moving across a solid surface: the slip length, which is defined as the ratio of slip velocity to shear rate at the wall, is a measure of the drag of the surface on the fluid. Slip lengths are typically of order a few nanometers and therefore can be taken as zero in a macroscopic channel (the no-slip boundary condition). However the degree of slip becomes increasingly important as chan-

nels are miniaturised. Recall that the average velocity of a liquid flowing through a channel $v \propto h^2 \nabla P$, where h is the height of the channel and ∇P is the pressure gradient that sets up the flow. As channel sizes are reduced an increasingly large pressure gradient is needed for a given throughput velocity. This can be alleviated by increasing the slip length at the channel walls.

For a smooth solid surface, the slip length increases as the wettability of the surface decreases [74]. However, its magnitude remains of order nanometers and therefore is of no real significance except for tiny channels. In this subsection, we

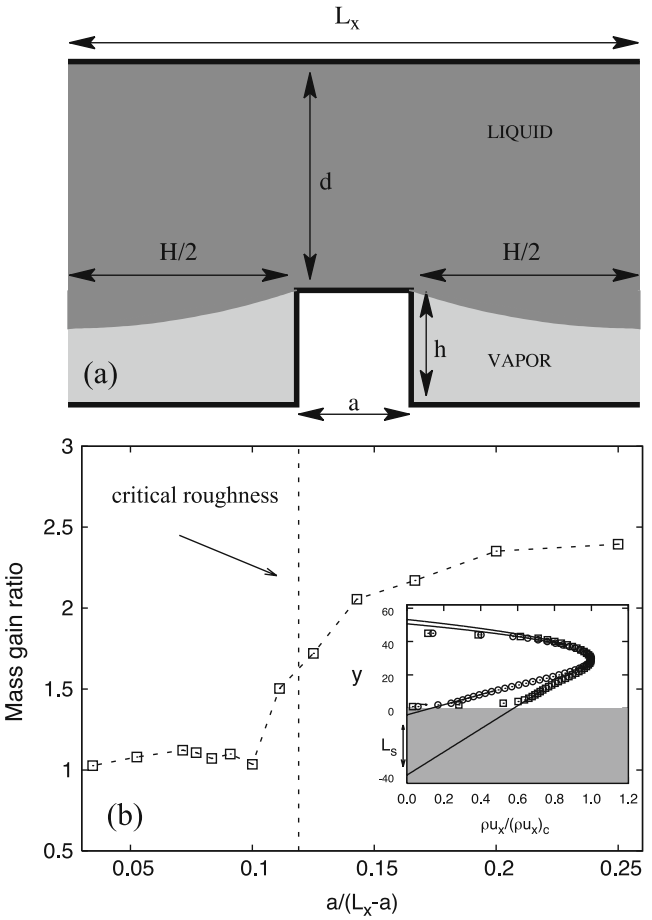

Fig. 11.15 (**a**) The geometry used to simulate flow over a superhydrophobic surface. The simulation parameters were: $h = 14$, $L_y = 45$, $L_x = 90$, and $\theta_e = 160°$. (**b**) Mass flow rate (normalised to the collapsed state) as a function of the effective roughness $a/(L_x - a)$. *inset*: Momentum profile for a suspended and a collapsed state. Both momentum profiles are shown for $x/L_x = 0.1$ and normalised to their center channel values. The *straight lines* correspond to extrapolations of the profiles to beyond the boundaries. Adapted figures with permission from Sbragaglia, et al. [77]. Copyright (2006) by the American Physical Society

will present results that show that a slip length of the order of microns might be induced by trapping the flowing fluid in the suspended state [75, 76]. The crucial idea is that the substrate acts as a composite of liquid–gas (perfect slip) and liquid–solid (no slip) areas and hence, the larger the liquid–gas section, the larger the slip length.

Results from simulations by Sbragaglia et al. [77] are shown in Fig. 11.15. They found that there is a critical roughness above which the mass flow rate through a microchannel increases significantly. This is because the fluid is in the suspended or collapsed state, above or below the critical roughness. The inset in Fig. 11.15 depicts the typical velocity profiles in the two states.

Further research [78, 79], however, has found that the shape of the liquid–gas interface plays an important role in determining the value of the slip length. The curvature of this interface leads to extra viscous dissipation which negates any advantage it might provide in the first place. Designing surface geometries where the slip length can be increased remains a major challenge.

11.7.3 The Transition from the Suspended to the Collapsed State on Superhydrophobic Surfaces

Given that the suspended and collapsed states have different dynamical behaviours, it is important to understand how and when the collapsed and suspended states are metastable or stable and to describe mechanisms for transitions between them.

For a given drop volume, the drop free energy increases with contact angle. This implies that the Cassie-Baxter state has the lowest energy when $\theta_{\mathrm{CB}} < \theta_{\mathrm{W}}$ and, similarly, that the Wenzel state is the ground state for $\theta_{\mathrm{W}} < \theta_{\mathrm{CB}}$. However, in many cases, both states are local minima of the free energy and there is a finite energy barrier opposing the transition between them. The origin of the energy barrier is pinning of the contact line, similar to that discussed in Sect. 11.7.1. For a transition from the suspended to the collapsed state to occur, the contact angle formed by the liquid drop on the sides of the posts has to become equal to the advancing contact angle.

There are several ways in which the collapse transition can be induced. Firstly, one can apply an external pressure or force [39]. Alternatively, the work required to overcome the energy barrier may be provided by a finite impact velocity of the drop [80, 81].

The collapse transition can also be initiated by reducing the volume of the drop by, for example, evaporation. This increases the Laplace pressure inside the drop (recall that $\Delta P \propto 1/R$ where R is the drop radius) and hence the curvature of the interface beneath it. For short posts the interface then touches the surface beneath the posts and the transition can take place. For longer posts collapse occurs when the interface curvature becomes sufficiently large that the interface reaches the equilibrium contact angle on the post sides, and hence depins [82, 83].

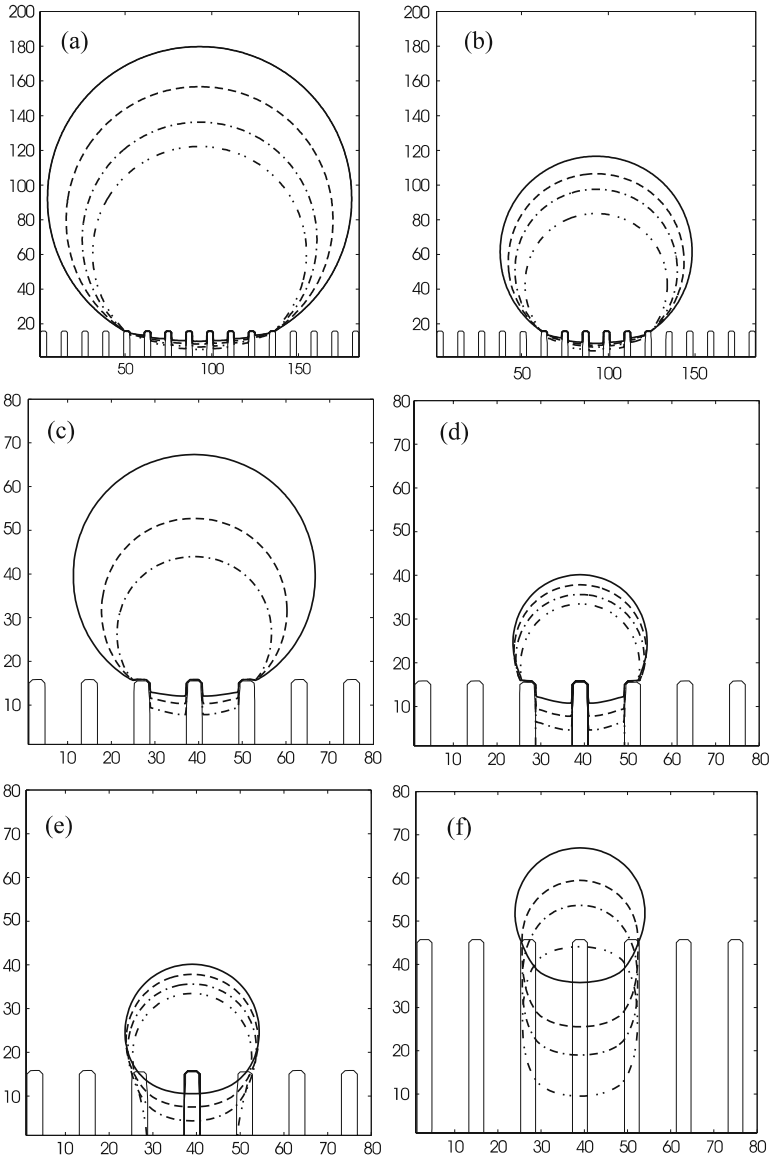

Fig. 11.16 Evolution of a cylindrical drop on a square array of posts of width $a = 3$, spacing $b = 9$ and height $l = 15$. (**a–c**) Evolution before collapse showing depinning of the receding contact line (note the scale change between (**b**) and (**c**)). (**d–f**) Motion of the collapsing drop: (**d**) cross sections in the plane bisecting the posts. (**e**) Same times as (**d**), but in the plane bisecting the gap between the posts. (**f**) Cross sections in the plane bisecting the gap, but with $l = 45$ to enable the collapse to be followed to later times. Adapted figures with permission from Kusumaatmaja et al. [82]

Figure 11.16 shows simulations indicating how the collapse transition proceeds for long posts as the liquid evaporates slowly. As the drop volume decreases it penetrates further into the gaps between the posts. However, movement down the posts is preempted by movement across the surface. The drop depins to lie on less posts, and the penetration is reduced. This continues until the drop lies on only three posts, when it eventually collapses.

It is useful to note that, to obtain the results in Fig. 11.16, we simulated a cylindrical drop on a square array of posts rather than a full, three dimensional, spherical drop. This allowed us to exploit the translational symmetry to reduce the system size to the repeat distance of the lattice in the third dimension, while preserving the important physics, in particular a two dimensional curvature of the interface between the posts.

11.8 Discussion

In this chapter we have concentrated on the use of lattice Boltzmann algorithms to study wetting and spreading. There are many other applications and areas for future research. We give some examples, inevitably selective, of interesting problems:

1. Different choices for the free energy can allow for new physics. A fruitful extensions is to include curvature terms which give lamellar phases [84] and vesicles[5] [85, 86].
2. Algorithmic advances, in particular those aimed at greater stability and the reduction of spurious velocities, will improve the ease of implementation of lattice Boltzmann codes. For example, hybrid algorithms, where the Navier-Stokes equation for the velocity field is solved using a lattice Boltzmann approach, but the convection-diffusion equation is treated using conventional finite difference techniques, are being developed. There has been work to develop the use of non-uniform grids [87, 88]. Entropic lattice Boltzmann models, which are unconditionally stable, are also possible [89, 90].
3. The lattice Boltzmann evolution equation can be viewed as the discretisation of a simplified Boltzmann equation and there is discussion as to whether it includes physics beyond that of the Navier Stokes equations [91–93]. Recent work has been successful in matching lattice Boltzmann and molecular dynamics simulations of simple fluids [94].
4. Including thermal fluctuations in a multiphase lattice Boltzmann method is still a major challenge [95, 96]. A simple approach is to include momentum-conserving random noise in the stress tensor. However, it was recently pointed out [95] that this method breaks down on small length scales.

[5] This work is in the context of phase field models, but the same free energy could be used within a binary lattice Boltzmann simulation.

5. The wetting and bounce back boundary conditions can be extended to cases where the solid surfaces themselves are mobile [31, 37]. The algorithm can then be used to study the dynamics of colloids in single- and multi-phase fluids [37, 97, 98].
6. A recent algorithm, coupling a lattice Boltzmann solvent to a molecular dynamics simulation of polymers is proving an exciting new tool for polymer hydrodynamics [99, 100]. Lattice Boltzmann has also been coupled to elastic filaments and membranes [101, 102]
7. Because lattice Boltzmann can handle tortuous boundaries it is particularly suited to simulating flow in porous materials [103–105] and to solving realistic models of blood flow [106, 107].
8. Lattice Boltzmann algorithms can be used to solve the equations of motion of more complex fluids, such as liquid crystals [108] and biologically active materials [109]. They provide a natural way of incorporating viscoelasticity.

The hydrodynamic equations of motion, together with an equilibrium corresponding to the minimum of a free energy, provide a realistic and elegant model of the wetting and spreading properties of multiphase fluids. Lattice Boltzmann algorithms are an effective tool to solve the continuum equations, helping us to understand wetting problems too complicated to be tractable analytically, and to motivate and interpret experiments.

References

1. T.M. Squires, S.R. Quake, Rev. Mod. Phys. **77**, 977 (2005)
2. W. Barthlott, C. Neinhuis, Planta **202**, 1 (1997)
3. A.R. Parker, C.R. Lawrence, Nature **414**, 33 (2001)
4. Y.M. Zheng, X.F. Gao, L. Jiang, Soft Matter **3**, 178 (2007)
5. P.G. de Gennes, Rev. Mod. Phys. **57**, 827 (1985)
6. D. Quéré, Annu. Rev. Fluid Mech. **38**, 71 (2008)
7. S. Herminghaus, M. Brinkmann, R. Seemann, Annu. Rev. Fluid Mech. **38**, 101 (2008)
8. R. Lipowsky, M. Brinkmann, R. Dimova, T. Franke, J. Kierfeld, X. Zhang, J. Phys.: Condens. Matter **17**, S537 (2005)
9. U. Frisch, B. Hasslacher, P. Pomeau, Phys. Rev. Lett. **56**, 1505 (1986)
10. S. Succi, *The Lattice Boltzmann Equation; for Fluid Dynamics and Beyond* (Oxford University Press, Oxford, 2001)
11. S. Chen, G.D. Doolen, Annu. Rev. Fluid Mech. **30**, 329 (1998)
12. R. Benzi, S. Succi, M. Vergassola, Phys. Rep. **222**, 145 (1992)
13. J.M. Yeomans, Physica A **369**, 159 (2006)
14. M.R. Swift, E. Orlandini, W.R. Osborn, J.M. Yeomans, Phys. Rev. E **54**, 5041 (1996)
15. X. Shan, H. Chen, Phys. Rev. E **49**, 2941 (1994)
16. A.K. Gunstensen, D.H. Rothman, S. Zaleski, G. Zanetti, Phys. Rev. A **43**, 4320 (1991)
17. A.J. Briant, J.M. Yeomans, Phys. Rev. E **69**, 031603 (2004)
18. C.M. Pooley, H. Kusumaatmaja, J.M. Yeomans, Phys. Rev. E **78**, 056709 (2008)
19. D. Jacqmin, J. Fluid Mech. **402**, 57 (2000)
20. P. Seppecher, Int. J. Eng. Sci. **34**, 977 (1996)
21. J. Cahn, J. Chem. Phys. **66**, 3667 (1977)
22. R. Cox, J. Fluid Mech. **168**, 169 (1986)

23. C. Huh, L. Scriven, J. Colloid Interf. Sci. **35**, 85 (1971)
24. T. Qian, X. Wang, P. Sheng, J. Fluid Mech. **564**, 333 (2006)
25. P. Bhatnagar, E. Gross, M. Krook, Phys. Rev. **94**, 511 (1954)
26. C. Pooley, K. Furtado, Phys. Rev. E **77**, 046702 (2008)
27. Z. Guo, C. Zheng, B. Shi, Phys. Rev. E **65**, 046308 (2002)
28. D. d'Humieres, I. Ginzburg, M. Krafczyk, P. Lallemand, L. Luo, Philos. Trans. R. Soc. A **360**, 437 (2002)
29. K. Premnath, J. Abraham, J. Comput. Phys. **224**, 539 (2007)
30. R. Du, B. Shi, X. Chen, Phys. Lett. A **359**, 564 (2006)
31. M. Bouzidi, M. Firdaouss, P. Lallemand, Phys. Fluid **13**, 3452 (2001)
32. I. Ginzburg, D. d'Humieres, Phys. Rev. E **68**, 066614 (2003)
33. R. Benzi, L. Biferale, M. Sbragaglia, S. Succi, F. Toschi, Phys. Rev. E **74**, 021509 (2006)
34. A. Wagner, Q. Li, Physica A **362**, 105 (2006)
35. D. Wolf-Gladrow, Lecture Notes in Mathematics, vol. 1725, chapter 5 (Springer-Verlag, Berlin, 2000)
36. S.S. Chikatamarla, I.V. Karlin, Comp. Phys. Comm. **179**, 140 (2008)
37. A. Ladd, R. Verberg, J. Stat. Phys. **104**, 1191 (2001)
38. J. Latt, B. Chopard, Phys. Rev. E **77**, 056703 (2008)
39. A. Dupuis, J.M. Yeomans, Langmuir **21**, 2624 (2005)
40. H. Kusumaatmaja, C.M. Pooley, J.M. Yeomans, Phys. Rev. E. **77**, 067301 (2008)
41. R. Ledesma-Aguilar, I. Pagonabarraga, A. Hernández-Machado, Phys. Fluid **19**, 102113 (2007)
42. A.J. Briant, A.J. Wagner, J.M. Yeomans, Phys. Rev. E **69**, 031602 (2004)
43. F. Diotallevi, L. Biferale, S. Chibbaro, G. Pontrelli, F. Toschi, S. Succi, Eur. Phys. J. Special Topics **171**, 237 (2009)
44. H. Kusumaatmaja, D.Phil. Thesis, University of Oxford, (2008)
45. H. Kusumaatmaja, A. Dupuis, J.M. Yeomans Europhys. Lett. **73**, 740 (2006)
46. R. Lucas, Kolloid-Z **23**, 15 (1918)
47. E. Washburn, Phys. Rev. **17**, 273 (1921)
48. M. Latva-Kokko, D.H. Rothman, Phys. Rev. Lett. **98**, 254503 (2007)
49. P. Saffman, G. Taylor, Proc. R. Soc. London Ser. A **245**, 312 (1958)
50. P. Tabeling, G. Zocchi, A. Libchaber, J. Fluid Mech. **177**, 67 (1987)
51. R. Ledesma-Aguilar, A. Hernández-Machado, I. Pagonabarraga, Phys. Fluid 19, 102112 (2007)
52. H. Gau, S. Hermingaus, P. Lenz, R. Lipowsky, Science **283**, 46 (1999)
53. A.A. Darhuber, S.M. Troian, S.M. Miller, S. Wagner, J. Appl. Phys. **87**, 7768 (2000)
54. J. Léopoldès, A. Dupuis, D.G. Bucknall, J.M. Yeomans, Langmuir **19**, 9818 (2003)
55. A. Dupuis, J. Léopoldès, J.M. Yeomans, Appl. Phys. Lett. **87**, 024103 (2005)
56. N.P. Sandreuter, Tappi J. **77**, 173 (1994)
57. H. Kusumaatmaja, J.M. Yeomans Langmuir **23**, 956 (2007)
58. D. Quéré, Rep. Prog. Phys. **68**, 2495 (2005)
59. X. Gao, L. Jiang, Nature **432**, 36 (2004)
60. A.B.D. Cassie, S. Baxter, Trans. Faraday Soc. **40**, 546 (1944)
61. D. Öner, T.J. McCarthy, Langmuir **16**, 7777 (2000)
62. J. Bico, C. Marzolin, D. Quéré, Europhys. Lett. **47**, 220 (1999)
63. U. Mock, R. Förster, W. Menz, R. Jürgen, J. Phys.: Condens. Matter **17**, S639 (2005)
64. A. Tuteja, W. Choi, M. Ma, J. Mabry, S. Mazzella, G. Rutledge, G. McKinley, R. Cohen, Science **318**, 1618 (2007)
65. L. Cao, T. Price, M. Weiss, D. Gao, Langmuir **24**, 1640 (2008)
66. R.N. Wenzel, Ind. Eng. Chem. **28**, 988 (1936)
67. J.F. Joanny, P.G. de Gennes, J. Chem. Phys. **81**, 552 (1984)
68. R.E. Johnson, R.H. Dettre, Adv. Chem. Ser. **43**, 112 (1964)
69. C. Huh, S.G. Mason, J. Coll. Int. Sci. **60**, 11 (1977)

70. J.F. Oliver, C. Huh, S.G. Mason, J. Coll. Int. Sci. **59**, 568 (1977)
71. J.W. Gibbs, Scientific Papers 1906. Dover reprint, Dover, NewYork (1961)
72. R. Shuttleworth, G.L.J. Bailey, Discuss. Faraday Soc. **3**, 16. (1948)
73. H. Kusumaatmaja, J.M. Yeomans, Langmuir **23**, 6019 (2007)
74. J.-L. Barrat, L. Bocquet, Faraday Discuss **112**, 119 (1999)
75. C. Cottin-Bizonne, E. Charlaix, L. Bocquet, J.-L. Barrat, Nature Mat. **2**, 237 (2003)
76. J. Ou, J.B. Perot, J.P. Rothstein, Phys. Fluids **17**, 103606 (2005)
77. M. Sbragaglia, R. Benzi, L. Biferale, S. Succi, F. Toschi, Phys. Rev. Lett. **97**, 204503 (2006)
78. J. Hyväluoma, J. Harting, Phys. Rev. Lett. **100**, 246001 (2008)
79. A. Steinberger, C. Cottin-Bizonne, P. Kleimann, E. Charlaix, Nature Mater. **6**, 665 (2007)
80. J. Hyväluoma, J. Timonen, Europhys. Lett. **83**, 64002 (2008)
81. D. Bartolo, F. Bouamrirene, É. Verneuil, A. Buguin, P. Silberzan, S. Moulinet, Europhys. Lett. **74**, 299 (2006)
82. H. Kusumaatmaja, M.L. Blow, A. Dupuis, J.M. Yeomans, Europhys. Lett. **81**, 36003 (2008)
83. M. Reyssat, J.M. Yeomans, D. Quéré, Europhys. Lett. **81**, 26006 (2008)
84. G. Gonnella, E. Orlandini, J.M. Yeomans, Phys. Rev. E **58**, 480 (1998)
85. D. Jamet, C. Misbah, Phys. Rev. E **76**, 051907 (2007)
86. D. Jamet, C. Misbah, Phys. Rev. E **78**, 031902 (2008)
87. X.Y. He, L.S. Luo, M. Dembo, J. Comp. Phys. **129**, 357 (1996)
88. O. Filippova, D. Hanel, J. Comp. Phys. **147**, 219 (1998)
89. B.M. Boghosian, J. Yepez, P.V. Coveney, A. Wagner, Proc. R. Soc. Lond. A **457**, 717 (2001)
90. S. Chikatamarla, S. Ansumali, I.V. Karlin, Phys. Rev. Lett. **97**, 010201 (2006)
91. X.B. Nie, G.D. Doolen, S.Y. Chen, J. Stat. Phys. **107**, 279 (2002)
92. F. Toschi, S. Succi, Europhys. Lett. **69**, 549 (2005)
93. Y.H. Zhang, R.S. Qin, D.R. Emerson, Phys. Rev. E **71**, 047702 (2005)
94. J. Horbach, S. Succi, Phys. Rev. Lett. **96**, 224503 (2006)
95. R. Adhikari, K. Stratford, M.E. Cates, A.J. Wagner, Europhys. Lett. **71**, 473 (2005)
96. B. Dünweg, U.D. Schiller, A.J.C. Ladd, Phys. Rev. E **76**, 036704 (2007)
97. K. Stratford, R. Adhikari, I. Pagonabarraga, J.C. Desplat, M.E. Cates, Science **2198**, 30 (2005)
98. M.E. Cates, J.C. Desplat, P. Stansell, A.J. Wagner, K. Stratford, R. Adhikari, I. Pagonabarraga, Phil. Trans. R. Soc. A **363**, 1917 (2005)
99. O.B. Usta, A.J.C. Ladd, J.E. Butler, J. Chem. Phys. **122**, 094902 (2005)
100. P. Ahlrichs, B. Dunweg, J. Chem. Phys. **111**, 8225 (1999)
101. A. Alexeev, R. Verberg, A.C. Balazs, Macromolecules **38**, 10244 (2005)
102. G.A. Buxton, R. Verberg, D. Jasnow, A.C. Balazs, Phys. Rev. E **71**, 056707 (2005)
103. B. Ferréol, D.H. Rothman, Transport in Porous Media **20**, 3 (1995)
104. R.J. Hill, D.L. Koch, A.J.C. Ladd, J. Fluid Mech. **448**, 243 (2001)
105. A. Koponen, D. Kandhai, E. Hellén, M. Alava, A. Hoekstra, M. Kataja, K. Niskanen, P. Sloot, J. Timonen, Phys. Rev. Lett. **80**, 716 (1998)
106. B. Chopard, R. Ouared, Int. J. Mod. Phys. C **18**, 712 (2007)
107. A.M. Artoli, A.G. Hoekstra, P.M.A. Sloot, J. Biomech. **39**, 873 (2006)
108. C. Denniston, D. Marenduzzo, E. Orlandini, J.M. Yeomans, Philos. Trans. R. Soc. A **362**, 1745 (2004)
109. D. Marenduzzo, E. Orlandini, J.M. Yeomans, Phys. Rev. Lett. **98**, 118102 (2007)